

# A full gap above the Fermi level: the charge density wave of monolayer VS<sub>2</sub>

Camiel van Efferen<sup>1\*</sup>, Jan Berges<sup>2</sup>, Joshua Hall<sup>1</sup>, Erik van Loon<sup>2</sup>, Stefan Kraus<sup>1</sup>, Arne Schobert<sup>2</sup>, Tobias Wekking<sup>1</sup>, Felix Huttmann<sup>1</sup>, Eline Plaar<sup>1</sup>, Nico Rothenbach<sup>3</sup>, Katharina Ollefs<sup>3</sup>, Lucas Machado Arruda<sup>4</sup>, Nick Brookes<sup>5</sup>, Gunnar Schönhoff<sup>2</sup>, Kurt Kummer<sup>5</sup>, Heiko Wende<sup>3</sup>, Tim Wehling<sup>2</sup>, Thomas Michely<sup>1</sup>

<sup>1</sup>*II. Physikalisches Institut, Universität zu Köln, Zùlpicher Straße 77, 50937 Köln, Germany*

<sup>2</sup>*Institut für Theoretische Physik, Bremen Center for Computational Materials Science, and MAPEX Center for Materials and Processes, Otto-Hahn-Allee 1, Universität Bremen, 28359 Bremen, Germany*

<sup>3</sup>*Fakultät für Physik und Center für Nanointegration Duisburg-Essen (CENIDE), Universität Duisburg-Essen, Carl-Benz-Straße, 47057 Duisburg, Germany*

<sup>4</sup>*Institut für Experimentalphysik, Freie Universität Berlin, Arnimallee 14, 14195 Berlin, Germany*

<sup>5</sup>*European Synchrotron Research Facility (ESRF), Avenue des Martyrs 71, CS 40220, 38043 Grenoble Cedex 9, France*

**In the standard model of charge density wave (CDW) transitions, the displacement along a single phonon mode lowers the total electronic energy by creating a gap at the Fermi level, making the CDW a metal–insulator transition. Here, using scanning tunneling microscopy and spectroscopy and *ab initio* calculations, we show that VS<sub>2</sub> realizes a CDW which stands out of this standard model. There is a full CDW gap residing in the unoccupied states of monolayer VS<sub>2</sub>. At the Fermi level, the CDW induces a topological metal-metal (Lifshitz) transition. Non-linear coupling of transverse and longitudinal phonons is essential for the formation of the CDW and the full gap above the Fermi level. Additionally, x-ray magnetic circular dichroism reveals the absence of net magnetization in this phase, pointing to coexisting charge and spin density waves in the ground state.**

The many-body ground states of two-dimensional (2D) materials, wherein the reduced dimensionality leads to the enhancement of correlation effects, have been extensively researched in recent years. Of particular interest are the coexistence or competition between charge density waves (CDWs), as found in many 2D transition metal dichalcogenides (TMDCs), with superconducting and magnetic phases<sup>1,2</sup>. Since these phases can be strongly dependent on the substrate<sup>3,4</sup> or the defect density<sup>5,6</sup>, the intrinsic properties of 2D materials are difficult to determine experimentally. In addition, CDWs themselves are the subject of an ongoing controversy regarding the driving force behind the CDW transition and the exact structure of the electronic system in the CDW phase of 2D materials<sup>7,8</sup>.

Peierls' explanation for the CDW in a one-dimensional chain of atoms states that periodic lattice distortions open an electronic gap at the nesting wavevector. This gap at the Fermi level lowers the energy of the occupied states and thus the total energy, while increasing the energy of the unoccupied states that do not contribute to the total energy. Thus, this gapping mechanism requires the gap to be at the Fermi level. However, in many (quasi-)2D cases, CDWs form in the

complete or partial absence of Fermi-surface nesting, suggesting that the driving mechanism behind their formation lies beyond a simple electronic disturbance<sup>9</sup>, and it has been questioned whether the concept of nesting is essential for understanding CDW formation<sup>10–12</sup>. Instead, a strong and wavevector-dependent electron–phonon coupling is often predicted to be the driving force behind the transition<sup>7</sup>. For these CDWs, spectral reconstructions are not limited to a small energy window around the Fermi energy, but can occur throughout the entire electronic structure, opening the door to novel spectral fingerprints of the CDW. A full gap could occur away from the Fermi energy. However, even for the well-studied strong-coupling TMDCs 2H-NbSe<sub>2</sub><sup>9,13,14</sup> and 1T-TaS<sub>2</sub><sup>7,15–17</sup>, no experimental verification of a clear CDW gap located away from the Fermi energy has been provided to date. Furthermore, at the Fermi energy, the undistorted phase and the CDW can have different Fermi-surface topologies, with the implication that the transition is a metal–metal Lifshitz transition<sup>18</sup>.

Metallic 1T-VS<sub>2</sub> is not only a promising electrode material in lithium-ion batteries<sup>19,20</sup>, but also a prototypical  $d^1$  system, expected to host strongly correlated physics<sup>21</sup>. It is stated to be a CDW material<sup>22,23</sup> and a candidate for 2D magnetism<sup>24,25</sup> with layer-dependent properties<sup>26</sup>, making it a model system for investigating complex ground states. Although difficult to synthesize, bulk 1T-VS<sub>2</sub> has been well studied, with many authors finding a  $(\sqrt{3} \times \sqrt{3})R30^\circ$  CDW transition at around 305 K when it was prepared via the de-intercalation of Li<sup>22,23,27–29</sup>. However, recent chemical vapour deposition grown samples and powder samples prepared under high pressure show no CDW transition<sup>30,31</sup>. Based on their finding of a phonon instability at a wavevector corresponding to the  $(\sqrt{3} \times \sqrt{3})R30^\circ$  CDW, Gauzzi *et al.* point out that bulk “VS<sub>2</sub> is at the verge of CDW transition”<sup>30</sup> but not a CDW material. Due to a similar difficulty in synthesis, the properties of monolayer 1T-VS<sub>2</sub> have proven equally elusive<sup>32</sup>. Theoretical calculations had predicted ferromagnetism and a CDW with a wavevector of  $2/3\bar{\Gamma}\bar{K}$ <sup>21,25</sup>. When it was first synthesized however, scanning tunneling microscope (STM) measurements did not reveal a CDW<sup>32</sup>, presumably due to strong hybridization with the Au(111) substrate, similar to the case of 2H-TaS<sub>2</sub> on Au(111)<sup>4,33,34</sup>.

Here we report the growth of VS<sub>2</sub> monolayers on the inert substrate graphene (Gr) on Ir(111) via a two-step molecular beam epitaxy (MBE) synthesis developed for sulfur-based TMDCs<sup>35</sup>. Using a combination of STM, scanning tunneling spectroscopy (STS), and *ab initio* density functional theory (DFT) calculations, we determine the spatial and electronic structure of monolayer VS<sub>2</sub>. We observe a  $\mathbf{q} \approx 2/3\bar{\Gamma}\bar{K}$  CDW as the electronic ground state at 7 K, which remains stable up to room temperature. A full gap in the density of states (DOS), residing completely in the unoccupied states, is measured via STS. From DFT and density functional perturbation theory (DFPT), we find that, although a transverse phonon mode initially becomes unstable in the harmonic approximation, the final CDW has a substantial admixture of longitudinal modes. The calculations are in excellent agreement with experiment, regarding both the electronic structure of the CDW phase and the spatial charge distribution observed on the VS<sub>2</sub> islands.

X-ray magnetic circular dichroism (XMCD) measurements at 7 K and 9 T robustly show vanishing total net magnetization. The coupling of the CDW to a spin density wave (SDW), energetically favored in DFT calculations, could explain this observation, providing interesting prospects for future research on the interplay of CDWs and magnetism.

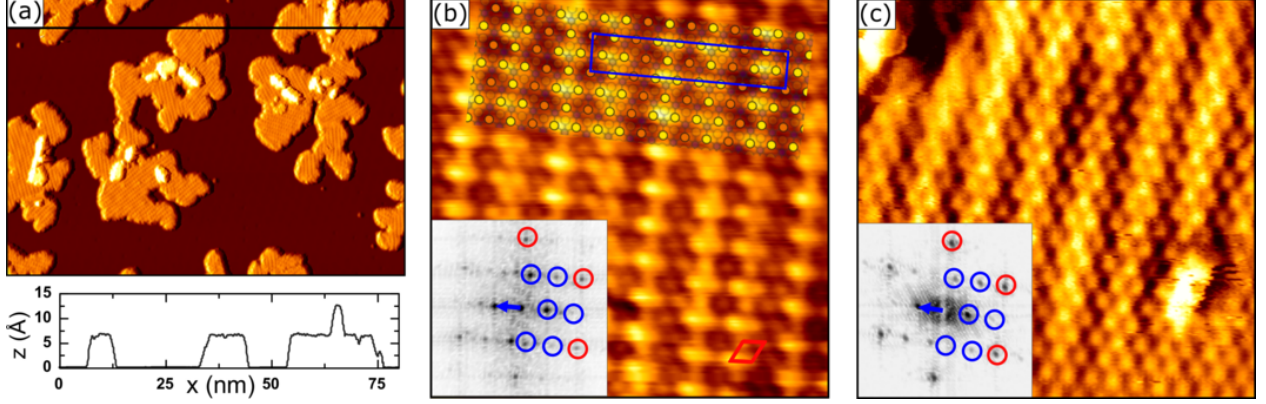


**Figure 1:** Structure of  $\text{VS}_2$  on Gr/Ir(111) at 7 K and 300 K. **a** Large-scale STM topograph of monolayer  $\text{VS}_2$  islands with small bilayers present. A height profile along the horizontal black line is shown below the image. **b, c** Atomically resolved STM images of monolayer  $\text{VS}_2$  at 7 K (**b**) and 300 K (**c**). The Fourier transform of each image is shown as an inset, with the  $1 \times 1$   $\text{VS}_2$  structure in red and the superstructure spots indicated in blue. In **b**, an atomic model for the  $9 \times \sqrt{3}R30^\circ$  superstructure is included as an overlay. The model depicts the top sulfur atoms, with their apparent height in STM coded in orange (low) and yellow (high). Measurement parameters: **a**  $80 \times 50 \text{ nm}^2$ ,  $I_t = 0.8 \text{ nA}$ ,  $V_t = -800 \text{ meV}$ , **b**  $6 \times 6 \text{ nm}^2$ ,  $I_t = 0.6 \text{ nA}$ ,  $V_t = 400 \text{ meV}$ , **c**  $6 \times 6 \text{ nm}^2$ ,  $I_t = 1.0 \text{ nA}$ ,  $V_t = -1000 \text{ meV}$ .

## Results

**CDW in monolayer  $\text{VS}_2$ .** The typical morphology of the MBE-grown monolayer  $\text{VS}_2$  islands on Gr/Ir(111) is shown in the large-scale STM image in Fig. 1a. The islands were grown by room-temperature deposition of vanadium in a sulfur background pressure of  $P_S^g = 1 \times 10^{-8} \text{ mbar}$  and subsequently annealed at 600 K in the same sulfur pressure. Annealing to temperatures of 800 K and above leads to the formation of a variety of sulfur-depleted phases, which are not under concern here. Similar observations were made by Arnold *et al.*<sup>32</sup>, who established monolayer stoichiometric 1T- $\text{VS}_2$  on Au(111) by annealing in a sulfiding gas at 670 K to 700 K, while sulfur-depleted monolayer phases form when annealed to the same or higher temperature in the absence of sulfiding species. We also note that depending on growth temperature and sulfur pressure bilayer samples without any monolayer islands evolve.

The monolayer islands are fully covered by a striped superstructure which is present regardless of island size or defect density and occurs in domains, typically separated by grain boundaries. In the topograph of Fig. 1b, taken at 7 K, the  $\text{VS}_2$  lattice is resolved, exhibiting the hexagonal arrangement of top layer sulfur atoms as protrusions. We find that monolayer  $\text{VS}_2$  has a lattice constant of  $a_{\text{VS}_2} = (3.21 \pm 0.02) \text{ \AA}$ , in good agreement with the bulk lattice constant of  $3.22 \text{ \AA}$  of 1T- $\text{VS}_2$ <sup>27,36</sup>. The similarity of the lattice constants indicates also the absence of epitaxial strain, consistent with the random orientation of the  $\text{VS}_2$  with respect to the Gr.

The stripes of the superstructure have an average periodicity of  $(2.28 \pm 0.02)a_{\text{VS}_2}$ . Close analogues to this structure have previously been observed in stoichiometric monolayer  $\text{VSe}_2$ .

There, a superstructure of identical symmetry is attributed to a CDW<sup>3,37–39</sup> [compare Fig. S1 in the Supplementary Information (SI)]. The superstructure is found to persist up to room temperature, as can be concluded from the STM topograph in Fig. 1c, taken at 300 K. At this temperature, the superstructure appears spontaneously only on larger islands, suggesting that the transition temperature between the superstructure and the undistorted phase is not far above room temperature. Indeed, on smaller islands the STM tip can be used to reversibly switch between the undistorted ( $1 \times 1$ ) structure and the superstructure, shown in Fig. S2 in the SI. This directly excludes the possibility that the superstructure is due to a sulfur-depleted phase. We conclude that the superstructure is most likely a CDW in a stoichiometric monolayer of 1T-VS<sub>2</sub>.

For the DFT calculations below, the experimental wave pattern must be approximated by a commensurate structure. A close approximation with periodicity  $2.25a_{\text{VS}_2}$  is overlaid on the atomic resolution image in Fig. 1b. It locally matches the incommensurate CDW quite well. The blue box indicates the corresponding  $9 \times \sqrt{3}R30^\circ$  unit cell. The Fourier transform of the topograph is shown as inset in Fig. 1b, with the wavevector of the CDW indicated (blue arrow). The same is done for the 300 K topograph in Fig. 1c. Within the margin of error, the wavevector is found to be temperature independent, with  $\mathbf{q}_{\text{CDW}(7\text{K})} = (0.656 \pm 0.006) \overline{\Gamma\text{K}}$  and  $\mathbf{q}_{\text{CDW}(300\text{K})} = (0.65 \pm 0.03) \overline{\Gamma\text{K}}$ . Since the wavevector of the  $9 \times \sqrt{3}R30^\circ$  unit cell,  $\mathbf{q}_{9 \times \sqrt{3}R30^\circ} = 2/3 \overline{\Gamma\text{K}} \approx 0.667 \overline{\Gamma\text{K}}$ , is slightly larger than the experimental value, we will in the following also consider another unit cell of size  $7 \times \sqrt{3}R30^\circ$ , with a slightly smaller wavevector  $\mathbf{q}_{7 \times \sqrt{3}R30^\circ} = 9/14 \overline{\Gamma\text{K}} \approx 0.643 \overline{\Gamma\text{K}}$ . With the experimental wavevector lying in between  $\mathbf{q}_{7 \times \sqrt{3}R30^\circ}$  and  $\mathbf{q}_{9 \times \sqrt{3}R30^\circ}$ , calculations with these two unit cells should capture the essential features of the incommensurate structure and provide a check on any artefacts or errors arising from using them for computational purposes (cf. Fig. S3 in the SI).

**Energetics of lattice instabilities.** *Ab initio* DFPT calculations of the acoustic phonon dispersion of undistorted monolayer 1T-VS<sub>2</sub> confirm that a structural instability and corresponding tendencies toward CDW formation exist for the experimental wavevector. Figure 2a shows that the longitudinal– and transverse–acoustic modes feature imaginary frequencies in several parts of the Brillouin zone. In other words, the Born–Oppenheimer energy surface is a downwards-opening parabola for small atomic displacements in the direction of these modes, as seen in Fig. 2b (triangle marks). At the experimental wavevector between  $\mathbf{q} = 2/3 \overline{\Gamma\text{K}}$  and  $\mathbf{q} = 9/14 \overline{\Gamma\text{K}}$ , we find an instability of the transverse–acoustic branch. However, the dominant instability within the harmonic approximation (i.e., DFPT), is located at  $\mathbf{q} = 1/2 \overline{\Gamma\text{M}}$  in the longitudinal–acoustic branch.

To go beyond the harmonic approximation, we have performed structural relaxations on appropriate unit cells. The resulting atomic positions are shown in Fig. 2c–e. On the aforementioned  $9 \times \sqrt{3}R30^\circ$  and  $7 \times \sqrt{3}R30^\circ$  unit cells, which can approximately host an integer multiple of the observed wavelength, the vanadium atoms are displaced from their symmetric positions by up to 8% of the lattice constant, while the positions of the sulfur atoms remain almost unchanged, see Fig. 2c, d. The associated energy gains amount to about 23 meV per VS<sub>2</sub> formula unit (cf. Ref. 21). The magnitude of these distortions and energy gains is similar to other octahedral TMDCs but exceeds by far what is found in trigonal–prismatic TMDCs<sup>7,40</sup>. For instance, on the DFT level, the maximum displacement in the  $\sqrt{13} \times \sqrt{13}$  CDW of 1T-NbSe<sub>2</sub> is 8.8% of the lattice constant with an energy gain of 57 meV per formula unit<sup>41</sup>, while in the  $3 \times 3$  CDW of 2H-NbSe<sub>2</sub> distortions and

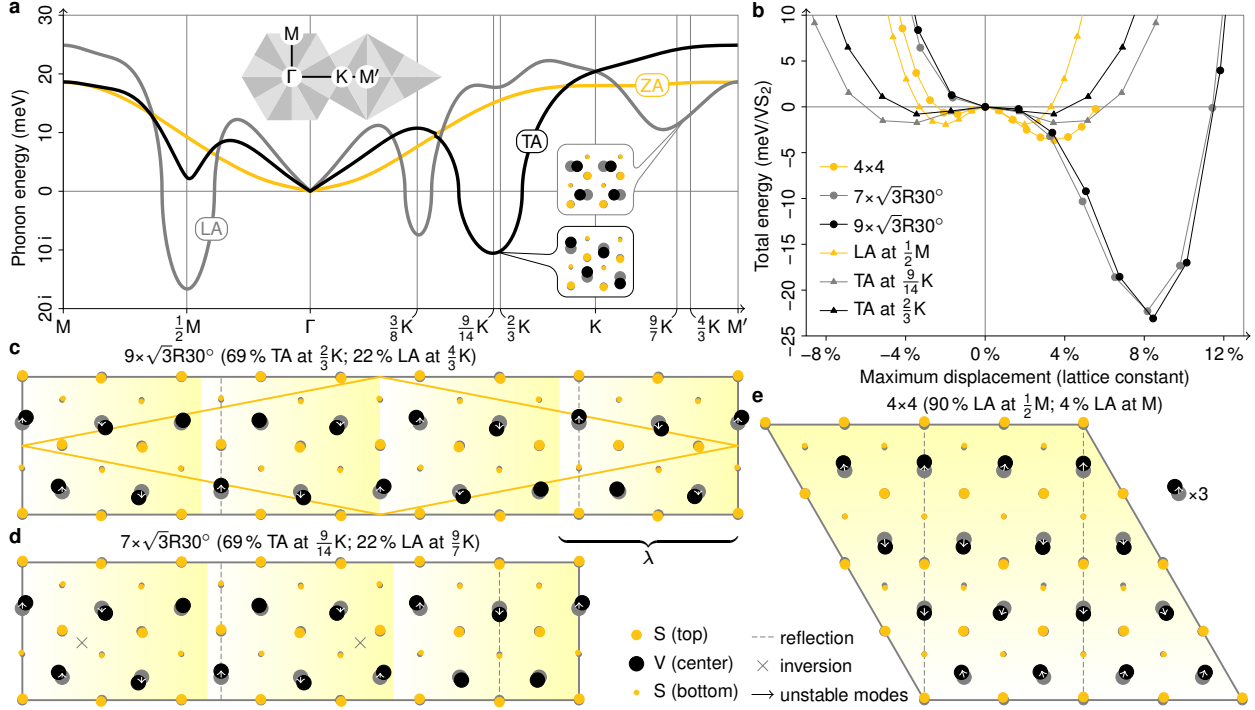


**Figure 2:** Lattice instabilities in monolayer 1T-VS<sub>2</sub> from first principles. **a** Acoustic phonon dispersion from DFPT. LA, TA, and ZA stand for dominant longitudinal, transverse, and out-of-plane atomic displacements. The insets show selected displacement patterns corresponding to indicated modes. **b** Total energy from DFT as a function of the displacement amplitude for atomic displacements toward relaxed crystal structures and their projections onto soft phonon modes. **c–e** Relaxed crystal structures on  $9 \times \sqrt{3}R30^\circ$ ,  $7 \times \sqrt{3}R30^\circ$ , and  $4 \times 4$  unit cells from DFT. Vanadium and sulfur atoms are represented by black and yellow dots, their undistorted positions by gray shadows. Arrows represent the projections of the atomic displacements onto soft phonon modes. (Only arrows longer than 2% of the lattice constant are shown.) The contributions of different phonon modes are quantified in the figure titles. The displacements in **c**, **d** are drawn to scale, those in **e** have been magnified by a factor of three for better visibility. The primitive cell of the structure in **c**, which is in agreement with the results of Ref. 21, is outlined in yellow. Dashed lines and crosses mark reflection planes and inversion centers.

energy gain amount to only 2.3% of the lattice constant and 3.7 meV per formula unit<sup>42</sup>.

The vanadium displacement has components in both the transverse and longitudinal direction (vertical and horizontal in Fig. 2c, d), even though the instability of the phonons at  $\mathbf{q} = 2/3\overline{\Gamma\text{K}}$  and  $\mathbf{q} = 9/14\overline{\Gamma\text{K}}$  is of transverse character (white arrows in Fig. 2c, d). As a consequence, all longitudinal displacement components must stem from non-linear mode–mode coupling beyond the harmonic approximation. The admixture of longitudinal displacement components stems mainly from wavevectors  $\mathbf{q} = 4/3\overline{\Gamma\text{K}}$  and  $\mathbf{q} = 9/7\overline{\Gamma\text{K}}$ , which are also commensurate with the  $9 \times \sqrt{3}R30^\circ$  and the  $7 \times \sqrt{3}R30^\circ$  unit cells, respectively. The admixed longitudinal modes at  $\mathbf{q} = 4/3\overline{\Gamma\text{K}}$  and

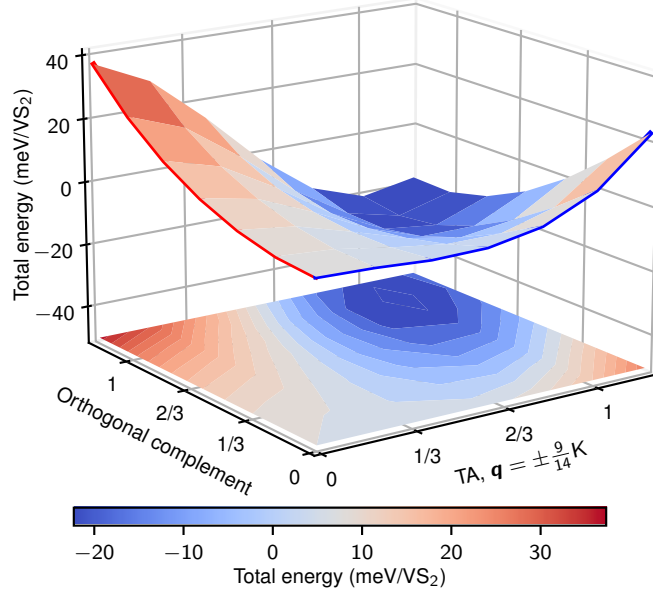


**Figure 3:** Born–Oppenheimer energy surface for the  $7 \times \sqrt{3}R30^\circ$  structure of  $1T\text{-VS}_2$ . The axes represent the projection of the full CDW displacement onto the transverse–acoustic phonon modes at  $\mathbf{q} = \pm 9/14 \overline{\Gamma K}$  and the orthogonal complement, which combines all other contributing modes. The full CDW displacement is located at the point (1, 1). The forces resulting from this energy surface are predominantly non-linear and coupled in both directions.

$\mathbf{q} = 9/7 \overline{\Gamma K}$  are stable in the harmonic approximation and the non-linear admixture is *not* related to any nesting or Peierls physics (cf. Fig. S4e, f in the SI).

We also find a distorted ground state on a  $4 \times 4$  unit cell, see Fig. 2e. This structure is commensurate to the six wavevectors  $\mathbf{q} = 1/2 \overline{\Gamma M}$ , where we have instabilities in the longitudinal–acoustic branch arising from near perfect Fermi-surface nesting, see Fig. S4a in the SI. However, here the displacements amount to only 4% of the lattice constant with a corresponding energy gain below 4 meV per  $1T\text{-VS}_2$  formula unit—much less than what is found for the  $7 \times \sqrt{3}R30^\circ$  or  $9 \times \sqrt{3}R30^\circ$  CDW structures. Thus, the DFT total energies of the fully relaxed structures are in line with the experimentally observed CDW patterns.

To illustrate the significance of the non-linear mode–mode coupling, in Fig. 2b, we also show the Born–Oppenheimer energy surfaces for displacements toward the relaxed structures (circle marks). The energy curve of the  $4 \times 4$  structure is steeper in the vicinity of the origin. In other words, the  $4 \times 4$  structure “wins” for small displacements. However, for larger displacements, the structures corresponding to the experimental wavevector reach by far the lowest values. These large energy gains at large displacements are inaccessible without non-linear mode–mode coupling, i.e., without the contribution of stable phonon modes (triangle marks). In the next section, we will address the non-linear regime of the distortions in a quantitative manner.

**Non-linear mode–mode coupling.** We decompose the entirety of atomic displacements of the relaxed  $7 \times \sqrt{3}R30^\circ$  structure as  $\mathbf{u} + \mathbf{v}$ , where  $\mathbf{u}$  points in the direction of the unstable transverse–

acoustic phonon modes at  $\mathbf{q} = \pm 9/14 \overline{\Gamma\text{K}}$  and the orthogonal complement  $\mathbf{v} \perp \mathbf{u}$  combines contributions from all other phonon modes. The unstable modes account for  $|\mathbf{u}|^2/|\mathbf{u} + \mathbf{v}|^2 \approx 69\%$  of the total displacement only. In Fig. 2b, we have already seen one-dimensional cross sections of the Born–Oppenheimer energy surface,  $E(\alpha\mathbf{u})$  and  $E(\beta(\mathbf{u} + \mathbf{v}))$ , where  $\alpha$  and  $\beta$  are dimensionless scaling factors. Now, we will consider the full 2D Born–Oppenheimer surface spanned by  $\mathbf{u}$  and  $\mathbf{v}$ . Figure 3 shows  $E(x\mathbf{u} + y\mathbf{v})$ , where the minimum at  $x = y = 1$  corresponds to the  $7 \times \sqrt{3}\text{R}30^\circ$  structure and  $x = y = 0$  is the undistorted structure. A fourth-order polynomial fit,

$$\frac{E(x\mathbf{u} + y\mathbf{v})}{\text{meV}/\text{VS}_2} \approx -25x^2 + 29y^2 + 34x^3 - 99x^2y - 20xy^2 - 12y^3 + 0.1x^4 + 44x^3y + 13x^2y^2 + 4.8xy^3 + 7.2y^4, \quad (1)$$

accurately describes the DFT Born Oppenheimer surface. Here, the first and second line give rise to linear and non-linear forces  $\mathbf{F} = -\nabla E$ , respectively. It turns out that the non-linear part of the forces is dominated by mode–mode coupled terms<sup>43–45</sup> (dependent on both  $x$  and  $y$ ). The energy reduction stems largely from the  $x^2y$  and  $xy^2$  terms above, which correspond to a shift of the minimum of the potential-energy surface toward finite positive  $y$  upon finite displacement in  $x$  direction and a softening of the effective spring constant in  $y$  direction for finite positive  $x$ , respectively. Note that within the harmonic approximation the  $x^2$  ( $y^2$ ) term lowers (raises) the energy.

The decisive role of mode–mode coupling terms  $x^2y$  and  $xy^2$  distinguishes 1T-VS<sub>2</sub> from systems like 2H-NbSe<sub>2</sub> or 2H-TaS<sub>2</sub>, where a single mode can be employed to describe anharmonicities, and distortions along a single effective coordinate suffice to explain the relaxation pattern of the full CDW and associated energy gains (cf. Fig. S5 in the SI).

The non-linear mode–mode coupling also manifests in monolayer 1T-VTe<sub>2</sub>, which is iso-electronic to monolayer 1T-VS<sub>2</sub>. Monolayer 1T-VTe<sub>2</sub> in experiment realizes a  $4 \times 4$  CDW<sup>46</sup> in contrast to monolayer 1T-VS<sub>2</sub>. In line with experiment, the comparison of DFT total energies in the fully relaxed supercells (Table S1 in the SI) reveals a clear preference of the  $4 \times 4$  structure in 1T-VTe<sub>2</sub>. At the harmonic level, this is likely related to a shift of the lattice instabilities, especially in the transverse–acoustic branch, toward smaller wavevectors in 1T-VTe<sub>2</sub> as compared to 1T-VS<sub>2</sub> (cf. Fig. 2a and Fig. S6a in the SI), which can be traced back to differences in the Fermi surface (cf. Figs. S4 and S6b–g in the SI). At the harmonic level, a CDW with  $7 \times \sqrt{3}\text{R}30^\circ$  structure of monolayer 1T-VS<sub>2</sub> is not expected, as Fig. S6a shows. The small energy gain and still appreciable distortions obtained from the relaxation of a  $7 \times \sqrt{3}\text{R}30^\circ$  structure of monolayer 1T-VS<sub>2</sub> (Table S1 in the SI) despite the stability on the harmonic level suggest that non-linear mode–mode coupling is also effective, here.

**Full CDW gap in the unoccupied states.** To better understand this CDW phase, we determined the electronic structure of monolayer VS<sub>2</sub> by a combination of STS experiments and simulated  $dI/dV$  maps based on the *ab initio* calculations using the  $7 \times \sqrt{3}\text{R}30^\circ$  and  $9 \times \sqrt{3}\text{R}30^\circ$  unit cells. STS spectra were used to locally probe the DOS of monolayer VS<sub>2</sub> at 7 K (black line) and 78.5 K (purple line), shown in Fig. 4a. Both spectra were taken with a clean Au tip in the middle of VS<sub>2</sub> islands. The most prominent feature is the gap located at about 0.175 eV, which is absent

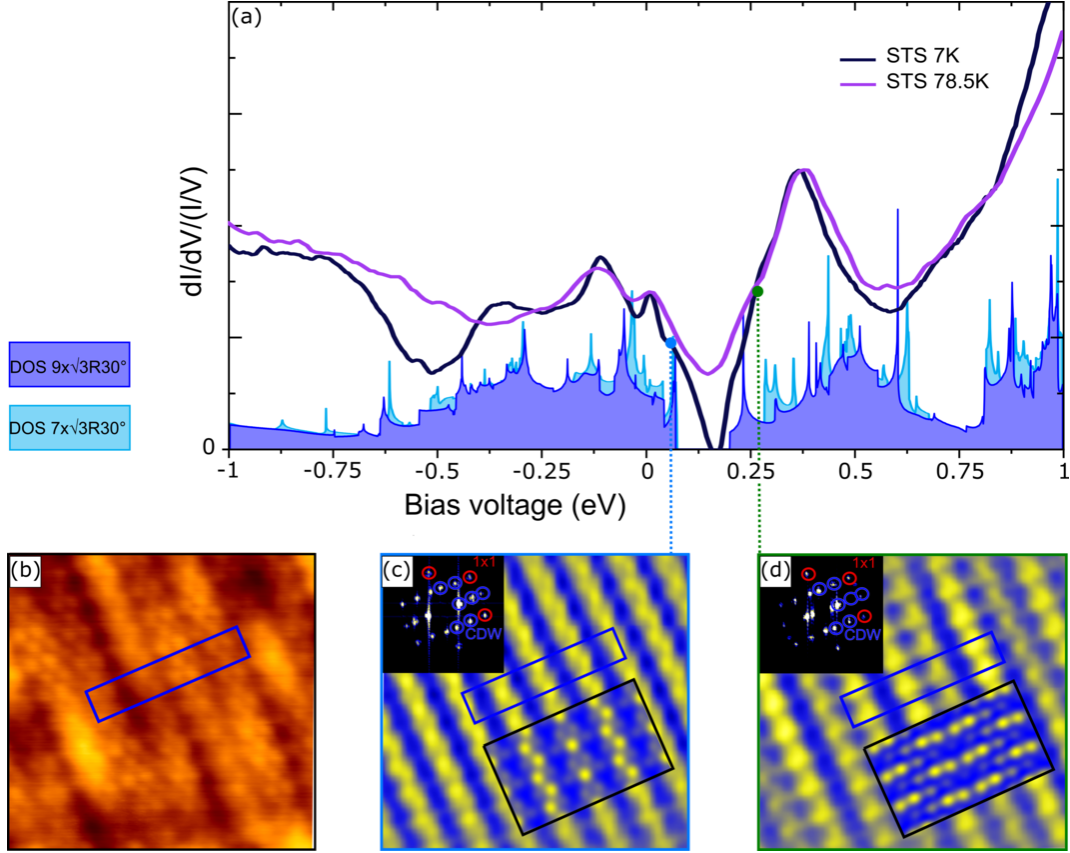


**Figure 4:** Spatially and electronically resolved CDW phase in monolayer  $\text{VS}_2$ . **a**  $dI/dV$  spectra taken with a Au tip on monolayer  $\text{VS}_2$  at 78.5 K (purple) and 7 K (black). The spectra are plotted along with the DFT-calculated DOS for the  $7 \times \sqrt{3}R30^\circ$  (cyan) and  $9 \times \sqrt{3}R30^\circ$  (indigo) CDW phases of monolayer  $1T\text{-VS}_2$ . **b** Atomically resolved STM topograph of monolayer  $\text{VS}_2$  taken at  $V_t = 175$  meV. **c, d** Fourier-filtered  $dI/dV$  conductance maps of the same region as in **b**, taken at  $V_t = 75$  meV (**c**) and  $V_t = 275$  meV (**d**). A linear yellow (maximum) to blue (minimum) color scale is used to depict the  $dI/dV$  intensity. The blue box indicates the same location in **b–d** and corresponds to a single  $9 \times \sqrt{3}R30^\circ$  unit cell of the CDW. In the same color scale, DFT-simulated  $dI/dV$  maps below (**c**) and above (**d**) the gap of the CDW are overlaid as insets. The maps show the integrated DOS from 0 meV to 137 meV (**c**) and from 137 meV to 275 meV (**d**). Additionally, the Fourier transforms of the conductance maps are shown in the upper-left corners with the  $1 \times 1$  (red) and CDW peaks (blue) highlighted by circles. Measurement parameters:  $f = 777.7$  Hz, **a**  $T = 78.5$  K,  $I_t = 0.3$  nA,  $V_{r.m.s.} = 6$  meV and  $T = 7$  K,  $I_t = 0.45$  nA,  $V_{r.m.s.} = 4$  meV, **b–d**  $T = 7$  K,  $5.5 \times 5.5$  nm<sup>2</sup>,  $I_t = 0.3$  nA,  $V_{r.m.s.} = 10$  meV.

in calculations of undistorted monolayer  $\text{VS}_2$ <sup>21</sup>. At 7 K, the  $dI/dV$  signal vanishes completely, corresponding to a full gap in the DOS. At 78.5 K, this gap is not fully open, appearing as a wide depression with a finite value at its minimum. In most other characteristic features the spectra agree qualitatively.

While the lack of energy resolution at 78.5 K certainly smears out the spectra and the gap, the reason for its absence is not immediately evident. When discussing the band structure below, it will be seen that the width and existence of the full gap depend on the magnitude of the lattice distortions, which may already be diminished at 78.5 K.



In the same figure, *ab initio* calculations for the DOS of VS<sub>2</sub>, structurally relaxed in the  $7 \times \sqrt{3}R30^\circ$  (cyan) or  $9 \times \sqrt{3}R30^\circ$  (indigo) unit cell, are shown. Both unit cells feature quite similar structures, as expected for close-lying  $\mathbf{q}$  vectors. Most striking, for both cases a full gap in the unoccupied states is predicted. They only differ in size: 0.13 eV and 0.21 eV for the  $9 \times \sqrt{3}R30^\circ$  and  $7 \times \sqrt{3}R30^\circ$  unit cell, respectively. The location of the gap matches the STS data. That the width of the gap in the spectrum is smaller than in DFT might stem from the ground-state calculation assumed in DFT, overestimating the vanadium atom displacement at realistic temperatures. Note also that while many of the characteristic features of calculated and measured DOS (peaks, minima) seem to agree, the experimental spectra appear to be compressed with respect to the DFT calculated DOS. This quasiparticle renormalization is indicative of strong electron–electron correlations beyond the approximations of DFT (compare Fig. S7 in the SI).

With theory and experiment largely agreeing on the electronic structure, we turn to the relation between the gap and the CDW measured on the VS<sub>2</sub> islands. For that purpose,  $dI/dV$  conductance maps were taken on either side of the gap (both in the unoccupied states), in the location shown in Fig. 4b. The maps help to distinguish structural from electronic contributions, providing a close approximation of the spatial distribution of the DOS at the selected energies. As shown in Fig. 4c, d, we find two different DOS distributions on either side of the gap (see Fig. S8 in the SI for the in-gap DOS). Both distributions are locked into the distorted lattice periodicity. They are out-of-phase, as seen in the blue unit cell drawn in the same location in Fig. 4b–d: The DOS maxima below the gap correspond to DOS minima above the gap and vice versa. This behavior is perfectly analogous to that for a CDW with a symmetric gap around the Fermi level<sup>4</sup>. Simulated  $dI/dV$  maps derived from the DFT DOS for a  $9 \times \sqrt{3}R30^\circ$  CDW are shown as an overlay in Fig. 4c, d. In Fig. 4c, the simulation reproduces both the alternating rows of single and zigzag atoms and the DOS minima between the rows. Its counterpart in Fig. 4d shows higher DOS contrast than experiment, but presents the same qualitative features. With the simulated maps based on the displacement patterns of Fig. 2c, the close agreement with experiment emphasizes the need to look beyond the harmonic approximation to understand this type of CDW.

**Band structure and Fermi-surface topology.** To deepen our understanding of the system, we calculated the spin-degenerate band structure, density of states, and Fermi surface of monolayer 1T-VS<sub>2</sub> with DFT. The results are shown in Fig. 5 and the Supplementary Videos. In the undistorted case, we find a single electronic band at the Fermi level, which strongly disperses between M and K and features a Van Hove singularity in the unoccupied states, as shown in Fig. 5a. The Fermi surface, depicted in Fig. 5b, consists of cigar-shaped electron pockets around the M points. For small distortions, partial gaps open at the Fermi level (e.g., between M and K). With increasing amplitude of the distortion, the gaps become larger and the bands are heavily reconstructed also for high energies. Only then, a full gap as observed in STS at 7 K emerges (cf. Supplementary Video 1).

The presence of the CDW is therefore in the first place correlated with the gap between M and K, which opens already for small displacements and results in a partial gapping of the total DOS. Presumably it is the associated gain in electronic energy that initially drives the CDW transition. Since the full gap only starts to open at 70 % of the final displacements, the experimental observation of a full gap above the Fermi level is an indication that the displacements in the experiments do not

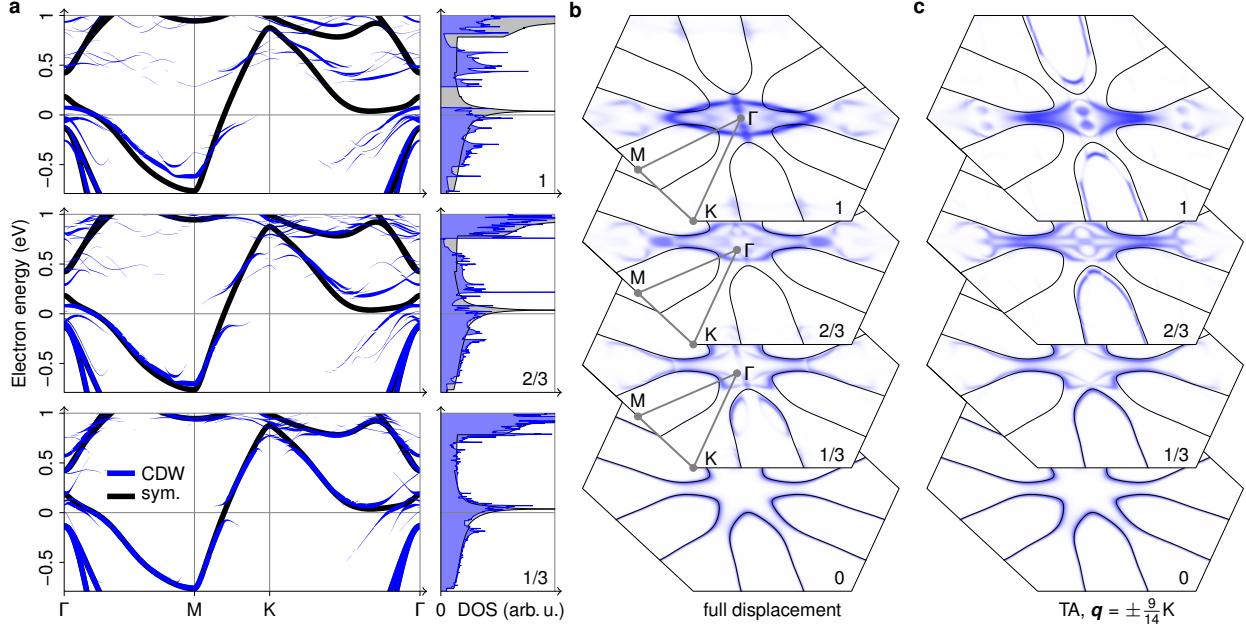


**Figure 5:** Electronic structure of monolayer 1T-VS<sub>2</sub> from DFT. Data for the undistorted structure and the  $7 \times \sqrt{3}R30^\circ$  CDW is shown in black and blue, respectively. The CDW data has been unfolded to the Brillouin zone of the undistorted structure. Here, the linewidth/saturation corresponds to the overlap of CDW and undistorted wave functions for the same  $\mathbf{k}$  point. Analogous results for 1T-VSe<sub>2</sub> and the  $9 \times \sqrt{3}R30^\circ$  CDW are shown in Fig. S3 in the SI. **a** Electronic band structure and density of states for 0 %, 1/3, 2/3, and 100 % of the displacements of the relaxed CDW structure. Please note that since the CDW breaks the  $C_3$  symmetry, the chosen path, indicated in **b**, does not represent the full Brillouin zone. The bands along an extended path are shown in Fig. S9 in the SI. **b, c** Lifshitz transition. The Fermi surface is shown for displacements toward the relaxed CDW structure (**b**) and its projection onto unstable phonon modes (**c**). The Supplementary Videos 1 and 2 show animations of the transitions in **b** and **c**, respectively (including bands, DOS, and structures).

fall much below the calculated ones.

At the Fermi level, there is no complete gap even at large distortion, since the downwards-dispersing bands along  $\Gamma$ -M are only slightly shifted downwards and remain above the Fermi level near  $\Gamma$ . On the other hand, the originally flat portion of the band structure between  $\Gamma$  and K now disperses downwards and crosses the Fermi level. The preservation of states near  $\Gamma$  that “mask” the partial gap at the Fermi level can be understood in terms of band characters and degeneracies, as shown in Fig. S10 in the SI. Altogether, the Fermi surface is reconstructed and not completely destroyed by the lattice distortion. The CDW transition is thus a metal-metal Lifshitz transition with a change in Fermi-surface topology, instead of the usual metal-insulator Peierls transition.

As shown in Fig. 5c, we cannot understand this Fermi-surface reconstruction based on a single unstable mode: The displacements expected from the harmonic approximation ( $\mathbf{u}$  in Equation 1) only induce gaps in two-third of the cigar-shaped electron pockets (cf. Supplementary Video 2).

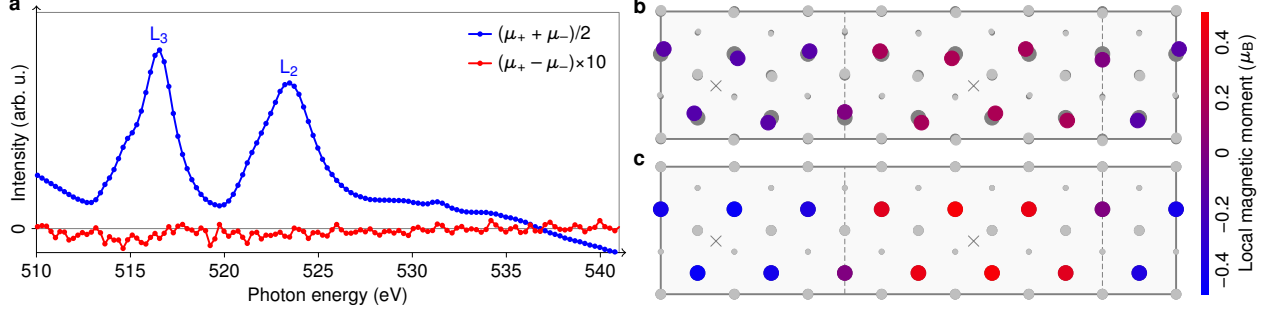


**Figure 6:** Magnetic properties of monolayer 1T-VS<sub>2</sub>. **a** Plotted in blue is the x-ray absorption signal averaged over both helicities and directions of the  $B$  field. The corresponding XMCD is shown in red. All measurements have been conducted in  $B$  fields of  $\pm 9$  T and at a temperature of 7 K. **b, c** Possible SDW pattern with **(b)** and without CDW **(c)**.

The other component  $v$  couples to segments of the Fermi surface that are not affected by  $u$ , i.e., the remaining third of the electron pockets (cf. Supplementary Video 3). Together, they transform the Fermi surface from multiple cigar-shaped electron pockets around the M points to the single elliptical hole pocket around  $\Gamma$  visible in Fig. 5b. The decomposition of the CDW contains modes at more than one wavevector  $\mathbf{q}$ , so several approximate Fermi-surface nesting conditions and electron-phonon coupling matrix elements play a role (Fig. S4b, c, e, f in the SI), enabling the CDW to affect distinct parts of the Fermi surface.

**Magnetic properties of monolayer VS<sub>2</sub>.** Prompted by the prediction of ferromagnetism for monolayer 1T-VS<sub>2</sub> in its  $\mathbf{q} = 2/3 \overline{\Gamma K}$  CDW phase<sup>21</sup>, we also examined the magnetic properties of VS<sub>2</sub>, by means of x-ray magnetic circular dichroism (XMCD). The monolayer VS<sub>2</sub> samples were grown *in situ* and investigated with STM beforehand to make sure that the same phase and decent coverage were obtained. A STM topograph of the sample investigated by XMCD is shown in Fig. S11 in the SI. The blue curve in Fig. 6 represents the x-ray absorption spectrum averaged over both helicities and external field directions. The overall line shape is very similar to previous bulk crystal measurements<sup>23</sup> and clearly fits to a  $3d^1$  configuration<sup>47</sup>. The red signal in Fig. 6 is the XMCD magnified by a factor of 10, where no signal above the noise level is visible. This implies that the total magnetization vanishes. Sum rule analysis would yield an upper bound of  $0.02\mu_B$  per vanadium atom. Since it cannot be strictly applied to the case of the  $V_{2,3}$  edges<sup>48</sup>, this analysis yields only a zero-order estimate of the upper bound, but we can safely conclude that neither ferromagnetic nor paramagnetic behavior is present in this system.

We investigated magnetic order in monolayer VS<sub>2</sub> using spin-polarized DFT. We were able to stabilize both ferromagnetic and SDW structures within the  $7 \times \sqrt{3}R30^\circ$  unit cell. In fact, magnetically ordered CDW phases are preferred over nonmagnetic CDW phases by energies of the order of 1 meV per VS<sub>2</sub> unit. Figure 6b shows the most favorable SDW pattern in the  $7 \times \sqrt{3}R30^\circ$  CDW phase. The magnetic moments on vanadium reach  $\pm 0.18\mu_B$ , those on sulfur only  $\pm 0.01\mu_B$  and are thus not shown. While the CDW alone reduces the total energy to  $-22.7$  meV per VS<sub>2</sub> unit with respect to the symmetric structure, the SDW lowers this value by another 1.5 meV to  $-24.2$  meV. Interestingly, without the CDW, a similar SDW with larger local moments of up to

$\pm 0.51\mu_B$  leads to an energy reduction of 7.1 meV. As already suggested by previous calculations of ferromagnetism in the  $9 \times \sqrt{3}R30^\circ$  structure of 1T-VS<sub>2</sub><sup>21</sup>, there is a competition between the lattice distortion and the formation of local moments. Although a full account of magnetism needs to go beyond the DFT level, in view of the good agreement between our *ab initio* results and the experimental STS and XMCD data, the formation of coupled CDW–SDW state in 1T-VS<sub>2</sub> is plausible. This presumption is further supported by comparison of the calculated DOS in the CDW–SDW state to the STS shown in Fig. S12 in the SI: the SDW formation on top of the CDW leads to a reduction of the gap size and the DOS of the coupled CDW–SDW is even in better agreement with the experiment than the non-spin-polarized CDW DOS.

## Discussion

Both the electronic and magnetic results for VS<sub>2</sub> shed some light on the properties of the isoelectronic compound VSe<sub>2</sub>, which displays a CDW of the same periodicity<sup>3,39,49</sup>. Our calculations strongly suggest that also for this system non-linear effects are relevant and that a full gap opens in the unoccupied states (compare Fig. S3 in the SI). A full gap at the Fermi level, as proposed for 1T-VSe<sub>2</sub><sup>6,39,49,50</sup>, would be unlikely to intrinsically occur for a CDW with the observed wavevector. The strong similarity between our calculations and experimental data, especially for those VSe<sub>2</sub> systems where only the  $7 \times \sqrt{3}R30^\circ$  CDW is observed<sup>37,38</sup>, lends credence to our analysis (compare Fig. S13 in the SI). It is possible that the simultaneous occurrence of a  $4 \times 1$  CDW<sup>3,6</sup>, perhaps due to substrate-induced strain<sup>51</sup>, causes an additional gap opening near the Fermi level as a result of the interplay between the CDWs. In any case, similar to VS<sub>2</sub>, the presence of a SDW coupled to the  $7 \times \sqrt{3}R30^\circ$  CDW could explain the absence of net magnetization in XMCD experiments<sup>38,39,49</sup>. Spin-polarized STM or XMLD might be able to detect the magnetic ground state for both VS<sub>2</sub> and VSe<sub>2</sub>.

In conclusion, VS<sub>2</sub> defies the common phenomenology of CDW formation, as the complete CDW gap occurs above the Fermi level, there is giant non-linear longitudinal–transverse mode–mode coupling, and the CDW formation is accompanied by a change of the Fermi-surface topology. The unconventional CDW appears to host further electronic correlations as signalled by the quasiparticle renormalization and magnetic-moment formation. In this respect, it is reminiscent of correlated phases in superlattice structures such as Star of David phases<sup>7</sup>, moiré superlattices<sup>52</sup>, and doped cuprate superconductors<sup>53</sup>. In the latter class, lattice anharmonicities are central to boosting superconductivity under THz optical driving<sup>45</sup>. The case of VS<sub>2</sub> presents new terrain: A metal–metal Lifshitz transition from non-linear electron–lattice effects in the strong-coupling regime is intertwined with electronic correlations. We note that the full gap in the DOS, situated within 0.2 eV from the Fermi level, opens up the possibility of inducing a metal–insulator transition upon mild gating or doping (e.g., with Li). Finally, we are convinced that the excellent agreement of experiment and theory for the unconventional CDW of monolayer VS<sub>2</sub> with the full gap in the unoccupied states provides a paradigmatic case study of strong-coupling CDWs in general.

## Methods

The Ir(111) crystal is cleaned by grazing incidence 1.5 keV Ar<sup>+</sup> ion exposure and flash annealing to 1500 K. A closed monolayer of single-crystalline Gr on Ir(111) is grown by room temperature exposure of Ir(111) to ethylene until saturation, subsequent annealing to 1300 K, followed by exposure to 200 L ethylene at 1300 K<sup>54</sup>.

The synthesis of vanadium sulfides on Gr/Ir(111) is based on a two-step MBE approach introduced in detail in Ref. 35 for MoS<sub>2</sub>. In the first step, the sample is held at room temperature and vanadium is evaporated at a rate of  $F_V = 2.5 \times 10^{16}$  atoms/(m<sup>2</sup>s) into a sulfur background pressure of  $P_S^g = 1 \times 10^{-8}$  mbar built up by thermal decomposition of pyrite inside a Knudsen cell. This results in dendritic TMDC islands of poor epitaxy. To make the islands larger and more compact, the sample is flashed in a sulfur background to 600 K.

The VS<sub>2</sub> layers were analyzed by STM, STS, and low-energy electron diffraction (LEED) inside a variable temperature (30 K to 700 K) ultrahigh vacuum apparatus and a low-temperature STM operating at 7 K and 78.5 K. The software WSXM<sup>55</sup> was used for STM data processing. XMCD measurements have been conducted at the beamline ID32 of the European Synchrotron Radiation Facility (ESRF) in Grenoble, France. The VS<sub>2</sub> samples were grown *in situ* inside the preparation chamber and checked with LEED and STM before x-ray absorption spectroscopy measurements. To be surface sensitive, the measurements were conducted in the total-electron-yield mode under normal incidence. The measurement temperature was 7 K and fields of 9 T were used. The spectra were recorded at the L<sub>3,2</sub> edges, i.e., using the dipole allowed transition from 2*p* states into the 3*d* shell potentially generating magnetism.

All DFT and DFPT calculations were performed using QUANTUM ESPRESSO<sup>56,57</sup>. We apply the PBE functional<sup>58,59</sup> and norm-conserving pseudopotentials from the PSEUDODOJO table<sup>60,61</sup>. In the undistorted case, uniform meshes (including  $\Gamma$ ) of  $12 \times 12$   $q$  and  $24 \times 24$   $k$  points are combined with a Fermi–Dirac smearing of 300 K. For a fixed unit-cell height of 15 Å, minimizing forces and in-plane pressure to below  $1 \times 10^{-5}$  Ry/Bohr and 0.1 kbar yields a lattice constant of 3.18 Å and a layer height (vertical sulfur–sulfur distance) of 2.93 Å. For the superstructure calculations, appropriate  $k$ -point meshes of similar density are chosen, except for the precise total energies quoted in the section about magnetism and in Table S1 in the SI, which required four times as dense meshes. The average lattice constant of superstructures is kept fixed at the value of the symmetric structure. Fourier interpolation to higher  $k$  resolutions ( $1000 \times 1000$  for calculations of the DOS) and the unfolding of electronic states is based on localized representations generated with WANNIER90<sup>62</sup>. For the visualization of the unfolded Fermi surfaces, a Fermi–Dirac broadening of 10 meV is used.

## Acknowledgments

This work was funded by the Deutsche Forschungsgemeinschaft (DFG, German Research foundation) through CRC 1238 (project no. 277146847, subprojects A01 and B06). J.B., A.S., and T.We.h. acknowledge financial support by the DFG through EXC 2077, GRK 2247, and SPP 2244. T.We.h. acknowledges support via the European Graphene Flagship Core3 Project (grant agreement 881603).

J.B., A.S., and T.We. acknowledge computational resources of the North-German Supercomputing Alliance (HLRN). E.v.L. is supported by the Central Research Development Fund of the University of Bremen. L.M.A. acknowledges financial support from CAPES (project no. 9469/13-3).

### Note on authorship

T.We. and T.M conceived this work and designed the research strategy. J.H. and discovered the CDW and developed, with the assistance of T.We., the growth method. C.v.E. and E.P. conducted and analyzed the STS experiments. J.B., A.S., and G.S., with support from E.v.L. and T.We., performed *ab initio* calculations. F.H. and S.K., with support from N.R., K.O., L.A., N.B., K.K., and H.W., performed and analyzed the XMCD experiment. The results were discussed by all authors. C.v.E., J.B., J.H., E.v.L., S.K., T.We., and T.M. wrote the manuscript with input from all authors. The first three authors have comparable contributions to this work.

### Competing interests

The authors declare no competing interests.

### Data availability

All the data and methods are present in the main text and the supplementary materials. Any other relevant data are available from the authors upon reasonable request.

### Code availability

Codes used in this work are available from the authors upon reasonable request.

### References

1. Ugeda, M. M. *et al.* Characterization of collective ground states in single-layer NbSe<sub>2</sub>. *Nat. Phys.* **12**, 92 (2016). URL <https://doi.org/10.1038/nphys3527>.
2. Zheng, B.-X. *et al.* Stripe order in the underdoped region of the two-dimensional Hubbard model. *Science* **358**, 1155 (2017). URL <https://doi.org/10.1126/science.aam7127>.
3. Duvjir, G. *et al.* Emergence of a metal–insulator transition and high-temperature charge-density waves in VSe<sub>2</sub> at the monolayer limit. *Nano Lett.* **18**, 5432 (2018). URL <https://doi.org/10.1021/acs.nanolett.8b01764>.
4. Hall, J. *et al.* Environmental control of charge density wave order in monolayer 2H-TaS<sub>2</sub>. *ACS Nano* **13**, 10210 (2019). URL <https://doi.org/10.1021/acsnano.9b03419>.
5. Yu, W. *et al.* Chemically exfoliated VSe<sub>2</sub> monolayers with room-temperature ferromagnetism. *Adv. Mater.* **31**, 1903779 (2019). URL <https://doi.org/10.1002/adma.201903779>.

6. Chua, R. *et al.* Can reconstructed Se-deficient line defects in monolayer VSe<sub>2</sub> induce magnetism? *Adv. Mater.* **32**, 2000693 (2020). URL <https://doi.org/10.1002/adma.202000693>.
7. Rossnagel, K. On the origin of charge-density waves in select layered transition-metal dichalcogenides. *J. Phys. Condens. Matter* **23**, 213001 (2011). URL <https://doi.org/10.1088/0953-8984/23/21/213001>.
8. Li, Y. W. *et al.* Folded superstructure and degeneracy-enhanced band gap in the weak-coupling charge density wave system 2H-TaSe<sub>2</sub>. *Phys. Rev. B* **97**, 115118 (2018). URL <https://doi.org/10.1103/PhysRevB.97.115118>.
9. Zhu, X., Guo, J., Zhang, J. & Plummer, E. W. Misconceptions associated with the origin of charge density waves. *Adv. Phys. X* **2**, 622 (2017). URL <https://doi.org/10.1080/23746149.2017.1343098>.
10. Johannes, M. D. & Mazin, I. I. Fermi surface nesting and the origin of charge density waves in metals. *Phys. Rev. B* **77**, 165135 (2008). URL <https://doi.org/10.1103/PhysRevB.77.165135>.
11. Inosov, D. S. *et al.* Fermi surface nesting in several transition metal dichalcogenides. *New J. Phys.* **10**, 125027 (2008). URL <https://doi.org/10.1088/1367-2630/10/12/125027>.
12. Berges, J., van Loon, E. G. C. P., Schobert, A., Rösner, M. & Wehling, T. O. Ab initio phonon self-energies and fluctuation diagnostics of phonon anomalies: Lattice instabilities from Dirac pseudospin physics in transition metal dichalcogenides. *Phys. Rev. B* **101**, 155107 (2020). URL <https://doi.org/10.1103/PhysRevB.101.155107>.
13. Borisenko, S. V. *et al.* Two energy gaps and Fermi-surface “arcs” in NbSe<sub>2</sub>. *Phys. Rev. Lett.* **102**, 166402 (2009). URL <https://doi.org/10.1103/PhysRevLett.102.166402>.
14. Weber, F. *et al.* Extended phonon collapse and the origin of the charge-density wave in 2H-NbSe<sub>2</sub>. *Phys. Rev. Lett.* **107**, 107403 (2011). URL <https://doi.org/10.1103/PhysRevLett.107.107403>.
15. Dardel, B. *et al.* Temperature-dependent pseudogap and electron localization in 1T-TaS<sub>2</sub>. *Phys. Rev. B* **45**, 1462 (1992). URL <https://doi.org/10.1103/PhysRevB.45.1462>.
16. Dardel, B. *et al.* Spectroscopic signatures of phase transitions in a charge-density-wave system: 1T-TaS<sub>2</sub>. *Phys. Rev. B* **46**, 7407 (1992). URL <https://doi.org/10.1103/PhysRevB.46.7407>.
17. Zwick, F. *et al.* Spectral consequences of broken phase coherence in 1T-TaS<sub>2</sub>. *Phys. Rev. Lett.* **81**, 1058 (1998). URL <https://doi.org/10.1103/PhysRevLett.81.1058>.

18. Lifshitz, I. M. Anomalies of electron characteristics of a metal in the high pressure region. *Zh. Eksp. Teor. Fiz.* **38**, 1569 (1960). URL <http://www.jetp.ac.ru/cgi-bin/e/index/e/11/5/p1130?a=list>.
19. Ji, Q. *et al.* Metallic vanadium disulfide nanosheets as a platform material for multifunctional electrode applications. *Nano Lett.* **17**, 4908 (2017). URL <https://doi.org/10.1021/acs.nanolett.7b01914>.
20. Li, Q., Zhou, Q., Shi, L., Chen, Q. & Wang, J. Recent advances in oxidation and degradation mechanisms of ultrathin 2D materials under ambient conditions and their passivation strategies. *J. Mater. Chem. A* **7**, 4291 (2019). URL <https://doi.org/10.1039/C8TA10306B>.
21. Isaacs, E. B. & Marianetti, C. A. Electronic correlations in monolayer VS<sub>2</sub>. *Phys. Rev. B* **94**, 035120 (2016). URL <https://doi.org/10.1103/PhysRevB.94.035120>.
22. Tsuda, T., Yasuoka, H., Kitaoka, Y. & Di Salvo, F. J. <sup>51</sup>V NMR study of the phase transition in 1T-VS<sub>2</sub>. *J. Magn. Magn. Mater.* **31-34**, 1101 (1983). URL [https://doi.org/10.1016/0304-8853\(83\)90816-8](https://doi.org/10.1016/0304-8853(83)90816-8).
23. Mulazzi, M. *et al.* Absence of nesting in the charge-density-wave system 1T-VS<sub>2</sub> as seen by photoelectron spectroscopy. *Phys. Rev. B* **82**, 075130 (2010). URL <https://doi.org/10.1103/PhysRevB.82.075130>.
24. Ma, Y. *et al.* Evidence of the existence of magnetism in pristine VX<sub>2</sub> monolayers (X = S, Se) and their strain-induced tunable magnetic properties. *ACS Nano* **6**, 1695 (2012). URL <https://doi.org/10.1021/nn204667z>.
25. Zhuang, H. L. & Hennig, R. G. Stability and magnetism of strongly correlated single-layer VS<sub>2</sub>. *Phys. Rev. B* **93**, 054429 (2016). URL <https://doi.org/10.1103/PhysRevB.93.054429>.
26. Zhang, H., Liu, L.-M. & Lau, W.-M. Dimension-dependent phase transition and magnetic properties of VS<sub>2</sub>. *J. Mater. Chem. A* **1**, 10821 (2013). URL <https://doi.org/10.1039/C3TA12098H>.
27. Murphy, D. W., Cros, C., Di Salvo, F. J. & Waszczak, J. V. Preparation and properties of Li<sub>x</sub>VS<sub>2</sub> (0 ≤ x ≤ 1). *Inorg. Chem.* **16**, 3027 (1977). URL <https://doi.org/10.1021/ic50178a008>.
28. Magonov, S., Contow, H.-J., Hillebrecht, H., Drechler, M. & Rotter, W. Atomic structure and superstructure of vanadium disulfide by scanning tunneling microscopy. *Optik* **83**, 60 (1989).
29. Sun, X. *et al.* In situ unravelling structural modulation across the charge-density-wave transition in vanadium disulfide. *Phys. Chem. Chem. Phys.* **17**, 13333 (2015). URL <https://doi.org/10.1039/C5CP01326G>.



30. Gauzzi, A. *et al.* Possible phase separation and weak localization in the absence of a charge-density wave in single-phase 1T-VS<sub>2</sub>. *Phys. Rev. B* **89**, 235125 (2014). URL <https://doi.org/10.1103/PhysRevB.89.235125>.
31. Hossain, M. *et al.* Chemical vapor deposition of 2D vanadium disulfide and diselenide and Raman characterization of the phase transitions. *Adv. Mater. Interfaces* **5**, 1800528 (2018). URL <https://doi.org/10.1002/admi.201800528>.
32. Arnold, F. *et al.* Novel single-layer vanadium sulphide phases. *2D Mater.* **5**, 045009 (2018). URL <https://doi.org/10.1088/2053-1583/aad0c8>.
33. Sanders, C. E. *et al.* Crystalline and electronic structure of single-layer TaS<sub>2</sub>. *Phys. Rev. B* **94**, 081404(R) (2016). URL <https://doi.org/10.1103/PhysRevB.94.081404>.
34. Lefcochilos-Fogelquist, H. M., Albertini, O. R. & Liu, A. Y. Substrate-induced suppression of charge density wave phase in monolayer 1H-TaS<sub>2</sub> on Au(111). *Phys. Rev. B* **99**, 174113 (2019). URL <https://doi.org/10.1103/PhysRevB.99.174113>.
35. Hall, J. *et al.* Molecular beam epitaxy of quasi-freestanding transition metal disulphide monolayers on van der Waals substrates: A growth study. *2D Mater.* **5**, 025005 (2018). URL <https://doi.org/10.1088/2053-1583/aaal5>.
36. Feng, J. *et al.* Metallic few-layered VS<sub>2</sub> ultrathin nanosheets: High two-dimensional conductivity for in-plane supercapacitors. *J. Am. Chem. Soc.* **133**, 17832 (2011). URL <https://doi.org/10.1021/ja207176c>.
37. Chen, P. *et al.* Unique gap structure and symmetry of the charge density wave in single-layer VSe<sub>2</sub>. *Phys. Rev. Lett.* **121**, 196402 (2018). URL <https://doi.org/10.1103/PhysRevLett.121.196402>.
38. Coelho, P. M. *et al.* Charge density wave state suppresses ferromagnetic ordering in VSe<sub>2</sub> monolayers. *J. Phys. Chem. C* **123**, 14089 (2019). URL <https://doi.org/10.1021/acs.jpcc.9b04281>.
39. Wong, P. K. J. *et al.* Evidence of spin frustration in a vanadium diselenide monolayer magnet. *Adv. Mater.* **31**, 1901185 (2019). URL <https://doi.org/10.1002/adma.201901185>.
40. Miller, D. C., Mahanti, S. D. & Duxbury, P. M. Charge density wave states in tantalum dichalcogenides. *Phys. Rev. B* **97**, 045133 (2018). URL <https://doi.org/10.1103/PhysRevB.97.045133>.
41. Calandra, M. Phonon-assisted magnetic Mott-insulating state in the charge density wave phase of single-layer 1T-NbSe<sub>2</sub>. *Phys. Rev. Lett.* **121**, 026401 (2018). URL <https://doi.org/10.1103/PhysRevLett.121.026401>.

42. Lian, C.-S., Si, C. & Duan, W. Unveiling charge-density wave, superconductivity, and their competitive nature in two-dimensional NbSe<sub>2</sub>. *Nano Lett.* **18**, 2924 (2018). URL <https://doi.org/10.1021/acs.nanolett.8b00237>.
43. Först, M. *et al.* Nonlinear phononics as an ultrafast route to lattice control. *Nat. Phys.* **7**, 854 (2011). URL <https://doi.org/10.1038/nphys2055>.
44. Truitt, P. A., Hertzberg, J. B., Altunkaya, E. & Schwab, K. C. Linear and nonlinear coupling between transverse modes of a nanomechanical resonator. *J. Appl. Phys.* **114**, 114307 (2013). URL <https://doi.org/10.1063/1.4821273>.
45. Mankowsky, R. *et al.* Nonlinear lattice dynamics as a basis for enhanced superconductivity in YBa<sub>2</sub>Cu<sub>3</sub>O<sub>6.5</sub>. *Nature* **516**, 71 (2014). URL <https://doi.org/10.1038/nature13875>.
46. Wang, Y. *et al.* Evidence of charge density wave with anisotropic gap in a monolayer VTe<sub>2</sub> film. *Phys. Rev. B* **100**, 241404 (2019). URL <https://doi.org/10.1103/PhysRevB.100.241404>.
47. Brik, M. G., Ogasawara, K., Ikeno, H. & Tanaka, I. Fully relativistic calculations of the L<sub>2,3</sub>-edge XANES spectra for vanadium oxides. *Eur. Phys. J. B* **51**, 345 (2006). URL <https://doi.org/10.1140/epjb/e2006-00243-5>.
48. Scherz, A. *et al.* Relation between L<sub>2,3</sub> XMCD and the magnetic ground-state properties for the early 3d element V. *Phys. Rev. B* **66**, 184401 (2002). URL <https://doi.org/10.1103/PhysRevB.66.184401>.
49. Feng, J. *et al.* Electronic structure and enhanced charge-density wave order of monolayer VSe<sub>2</sub>. *Nano Lett.* **18**, 4493 (2018). URL <https://doi.org/10.1021/acs.nanolett.8b01649>.
50. Bonilla, M. *et al.* Strong room-temperature ferromagnetism in VSe<sub>2</sub> monolayers on van der Waals substrates. *Nat. Nanotechnol.* **13**, 289 (2018). URL <https://doi.org/10.1038/s41565-018-0063-9>.
51. Si, J. G. *et al.* Origin of the multiple charge density wave order in 1T-VSe<sub>2</sub>. *Phys. Rev. B* **101**, 235405 (2020). URL <https://doi.org/10.1103/PhysRevB.101.235405>.
52. Cao, Y. *et al.* Correlated insulator behaviour at half-filling in magic-angle graphene superlattices. *Nature* **556**, 80 (2018). URL <https://doi.org/10.1038/nature26154>.
53. Tranquada, J. M., Sternlieb, B. J., Axe, J. D., Nakamura, Y. & Uchida, S. Evidence for stripe correlations of spins and holes in copper oxide superconductors. *Nature* **375**, 561 (1995). URL <https://doi.org/10.1038/375561a0>.
54. van Gastel, R. *et al.* Selecting a single orientation for millimeter sized graphene sheets. *Appl. Phys. Lett.* **95**, 121901 (2009). URL <https://doi.org/10.1063/1.3225554>.

55. Horcas, I. *et al.* WSXM: A software for scanning probe microscopy and a tool for nanotechnology. *Rev. Sci. Instrum.* **78**, 013705 (2007). URL <https://doi.org/10.1063/1.2432410>.
56. Giannozzi, P. *et al.* QUANTUM ESPRESSO: A modular and open-source software project for quantum simulations of materials. *J. Phys. Condens. Matter* **21**, 395502 (2009). URL <https://doi.org/10.1088/0953-8984/21/39/395502>.
57. Giannozzi, P. *et al.* Advanced capabilities for materials modelling with QUANTUM ESPRESSO. *J. Phys. Condens. Matter* **29**, 465901 (2017). URL <https://doi.org/10.1088/1361-648X/aa8f79>.
58. Perdew, J. P., Burke, K. & Ernzerhof, M. Generalized gradient approximation made simple. *Phys. Rev. Lett.* **77**, 3865 (1996). URL <https://doi.org/10.1103/PhysRevLett.77.3865>.
59. Perdew, J. P., Burke, K. & Ernzerhof, M. Generalized gradient approximation made simple [Phys. Rev. Lett. 77, 3865 (1996)]. *Phys. Rev. Lett.* **78**, 1396(E) (1997). URL <https://doi.org/10.1103/PhysRevLett.78.1396>.
60. Hamann, D. R. Optimized norm-conserving Vanderbilt pseudopotentials. *Phys. Rev. B* **88**, 085117 (2013). URL <https://doi.org/10.1103/PhysRevB.88.085117>.
61. van Setten, M. J. *et al.* The PseudoDojo: Training and grading a 85 element optimized norm-conserving pseudopotential table. *Comput. Phys. Commun.* **226**, 39 (2018). URL <https://doi.org/10.1016/j.cpc.2018.01.012>.
62. Mostofi, A. A. *et al.* An updated version of wannier90: A tool for obtaining maximally-localised Wannier functions. *Comput. Phys. Commun.* **185**, 2309 (2014). URL <https://doi.org/10.1016/j.cpc.2014.05.003>.

# Supplementary Information of “A full gap above the Fermi level: the charge density wave of monolayer VS<sub>2</sub>”

Camiel van Efferen<sup>1\*</sup>, Jan Berges<sup>2</sup>, Joshua Hall<sup>1</sup>, Erik van Loon<sup>2</sup>, Stefan Kraus<sup>1</sup>, Arne Schobert<sup>2</sup>, Tobias Wekking<sup>1</sup>, Felix Huttmann<sup>1</sup>, Eline Plaar<sup>1</sup>, Nico Rothenbach<sup>3</sup>, Katharina Ollefs<sup>3</sup>, Lucas Machado Arruda<sup>4</sup>, Nick Brookes<sup>5</sup>, Gunnar Schönhoff<sup>2</sup>, Kurt Kummer<sup>5</sup>, Heiko Wende<sup>3</sup>, Tim Wehling<sup>2</sup>, Thomas Michely<sup>1</sup>

<sup>1</sup>*II. Physikalisches Institut, Universität zu Köln, Zùlpicher Straße 77, 50937 Köln, Germany*

<sup>2</sup>*Institut für Theoretische Physik, Bremen Center for Computational Materials Science, and MAPEX Center for Materials and Processes, Otto-Hahn-Allee 1, Universität Bremen, 28359 Bremen, Germany*

<sup>3</sup>*Fakultät für Physik und Center für Nanointegration Duisburg-Essen (CENIDE), Universität Duisburg-Essen, Carl-Benz-Straße, 47057 Duisburg, Germany*

<sup>4</sup>*Institut für Experimentalphysik, Freie Universität Berlin, Arnimallee 14, 14195 Berlin, Germany*

<sup>5</sup>*European Synchrotron Research Facility (ESRF), Avenue des Martyrs 71, CS 40220, 38043 Grenoble Cedex 9, France*

**Figure S1: Unit cells**

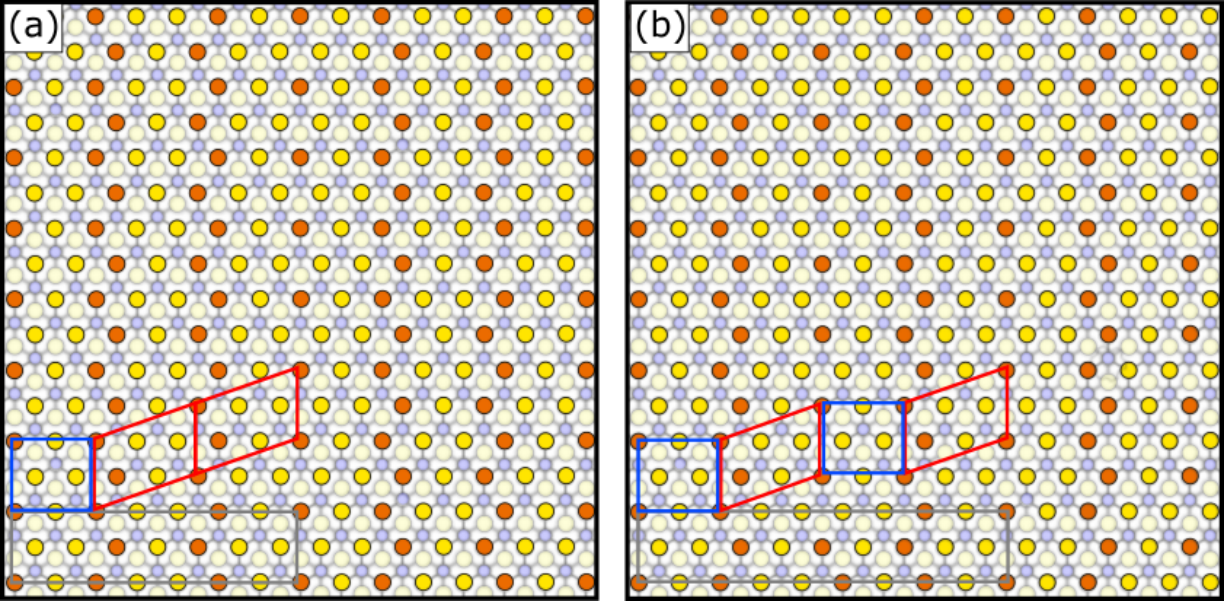


**Figure S1:** Correspondence between unit cells in monolayer  $VSe_2$  literature and the unit cells used in this paper. In **a** and **b**, models of the 1T- $VS_2$  atomic lattice are depicted with V atoms in blue and bottom-S atoms in faint yellow.  $7 \times \sqrt{3}R30^\circ$  (**a**) and  $9 \times \sqrt{3}R30^\circ$  (**b**) superstructures are visible in the top-S atoms, which are drawn in two colors to mimic the experimental apparent height in yellow (bright) and orange (dark). The dark gray rectangles indicate the  $7 \times \sqrt{3}R30^\circ$  (**a**) and  $9 \times \sqrt{3}R30^\circ$  (**b**) unit cells. The blue rectangle is a  $2 \times \sqrt{3}R30^\circ$  unit, the red rhombus a  $\sqrt{7}R19.1^\circ \times \sqrt{3}R30^\circ$ .

In the isotypic material  $VSe_2$ , a superstructure of same symmetry as in  $VS_2$ , has been identified and attributed to a charge density wave (CDW)<sup>1-4</sup>. In these studies, the superstructure was described by a combination of  $2 \times \sqrt{3}R30^\circ$  and  $\sqrt{7}R19.1^\circ \times \sqrt{3}R30^\circ$  units, which we mark in our model in Fig. S1a, b in blue and red, respectively. By the combination of a single  $2 \times \sqrt{3}R30^\circ$  and two  $\sqrt{7}R19.1^\circ \times \sqrt{3}R30^\circ$  units, the  $7 \times \sqrt{3}R30^\circ$  CDW lattice can be described; two  $2 \times \sqrt{3}R30^\circ$  units and two  $\sqrt{7}R19.1^\circ \times \sqrt{3}R30^\circ$  units make up the  $9 \times \sqrt{3}R30^\circ$  lattice.

**Figure S2: Tip-induced switching between distorted and undistorted phase**

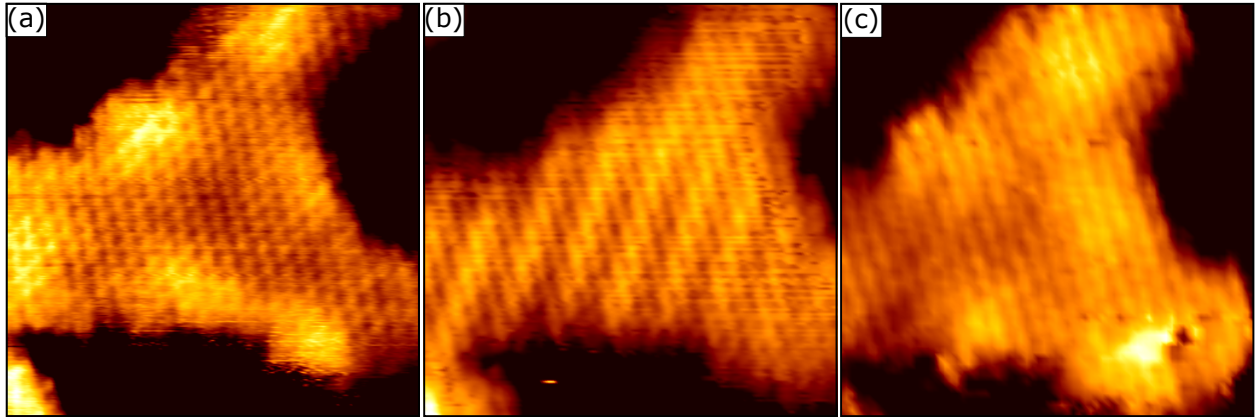


**Figure S2:** Influence of STM tip on monolayer  $\text{VS}_2$ : the two consecutive STM scans in panel **a** and **b** document the STM-tip-induced switch from the undistorted to the superstructure CDW phase. Scan **c** is taken 15 minutes later and shows no more signs of the superstructure. Images taken at 300 K. Measurement parameters: **a–c**  $7 \times 7 \text{ nm}^2$ ,  $I_t = 0.5 \text{ nA}$ ,  $V_t = -90 \text{ meV}$ .

The presence of the superstructure at room temperature can also be influenced by the scanning tunneling microscope (STM) tip. Figure S2a, b shows two consecutive STM scans, taken at the same position, tunnelling current, and bias. In Fig. S2a, the STM reveals only hexagonal atomic ordering inside the small  $\text{VS}_2$  structure. In the successive STM scan in Fig. S2b, the wave superstructure is observed in the same region, with the phase transition apparently triggered by the interaction with the STM tip. A subsequent STM scan taken about 15 minutes later, displayed in Fig. S2c, again shows the absence of the superstructure.

**Figure S3: 1T-VSe<sub>2</sub> vs 1T-VS<sub>2</sub> and  $9 \times \sqrt{3}R30^\circ$  vs  $7 \times \sqrt{3}R30^\circ$**

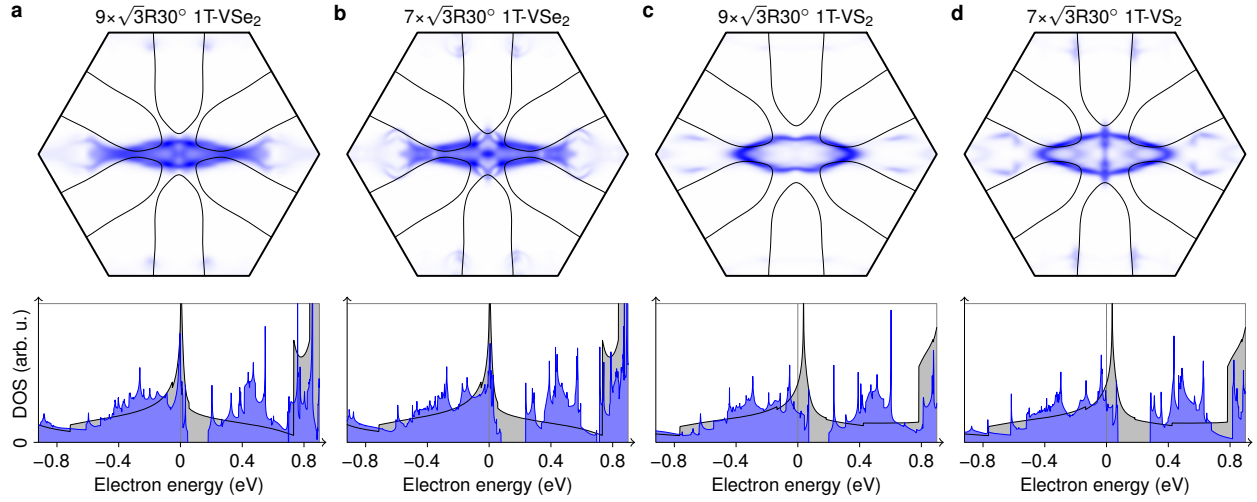


**Figure S3:** Fermi surface and DOS of monolayer **a, b** 1T-VSe<sub>2</sub> and **c, d** 1T-VS<sub>2</sub> in the undistorted phase as well as for the **a, c**  $9 \times \sqrt{3}R30^\circ$  and **b, d**  $7 \times \sqrt{3}R30^\circ$  CDW as obtained from DFT. The CDW data has been unfolded to the Brillouin zone of the undistorted structure. Here, the color saturation corresponds to the overlap of CDW and undistorted wave functions for the same  $\mathbf{k}$  point.

In Fig. S3a, b, we show the Fermi surface and density of states (DOS) of monolayer 1T-VSe<sub>2</sub> in the undistorted as well as  $9 \times \sqrt{3}R30^\circ$  and  $7 \times \sqrt{3}R30^\circ$  CDW phases from density functional theory (DFT). In VSe<sub>2</sub> a similar CDW as the one found in VS<sub>2</sub> has been reported repeatedly<sup>1,2,4-6</sup>. As points of reference, corresponding results for monolayer 1T-VS<sub>2</sub> are displayed in Fig. S3c, d. The results for the  $9 \times \sqrt{3}R30^\circ$  and  $7 \times \sqrt{3}R30^\circ$  cells agree qualitatively. Furthermore, our calculations suggest that 1T-VSe<sub>2</sub> and 1T-VS<sub>2</sub> are very similar in their electronic structure. In the distorted phase, 1T-VSe<sub>2</sub> will also have a full gap in the unoccupied states; at the Fermi energy, only a partial gap is expected. Though this has been observed in experiment<sup>2,3</sup>, most studies on monolayer VSe<sub>2</sub> agree on a full gap located at the Fermi level<sup>1,4,6,7</sup>. To our understanding, such a gap would require a filling of the downwards-dispersing bands near  $\Gamma$ , which are not gapped in the CDW configuration. According to our DFT calculations for both 1T-VS<sub>2</sub> and 1T-VSe<sub>2</sub> on a  $9 \times \sqrt{3}R30^\circ$  ( $7 \times \sqrt{3}R30^\circ$ ) supercell,  $1/9 \approx 0.11$  ( $1/7 \approx 0.14$ ) additional electrons would shift the gap to the Fermi energy (compare Fig. S10a, b). This charge could be provided by, e.g., the substrate or defects.

**Figure S4: Nesting conditions and electron–phonon coupling**

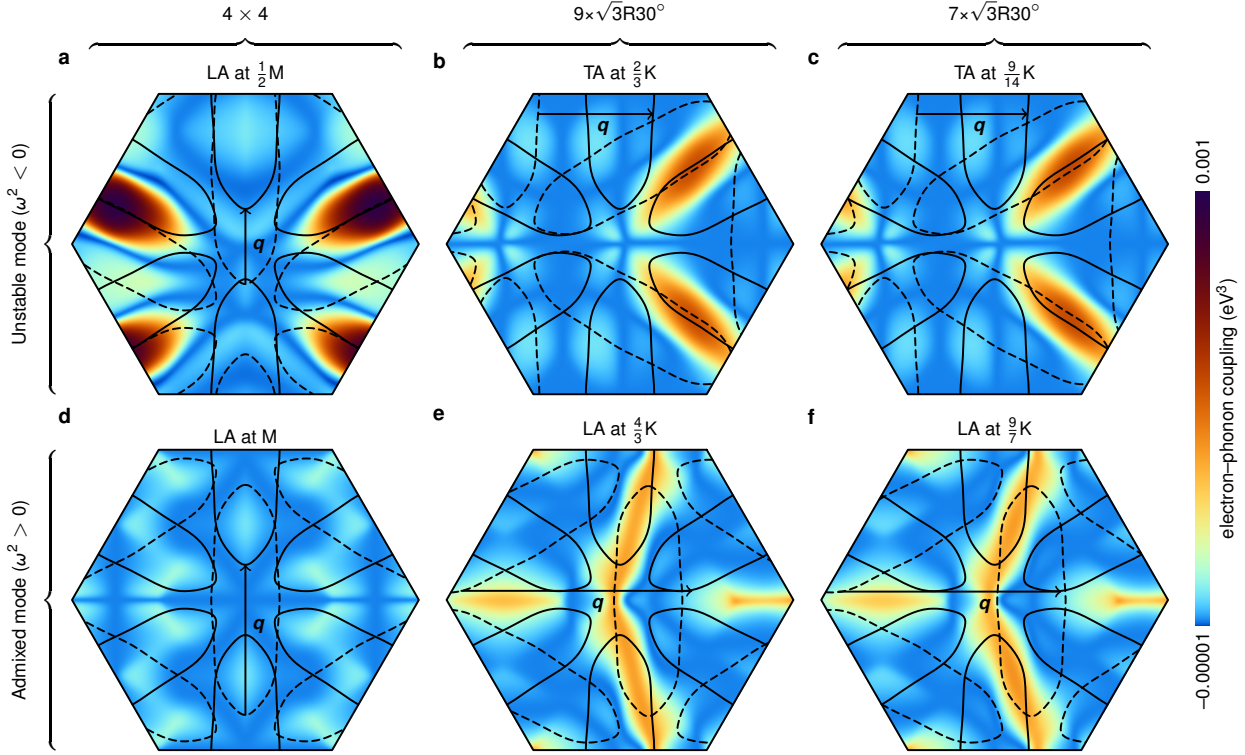


**Figure S4:** Nesting conditions for different phonon wavevectors  $q$ . We show the relevant electron–phonon coupling  $2\omega_q g_{k+q,k} \tilde{g}_{k,k+q}$  as a function of the electron wavevector  $k$  (color scale) together with the original Fermi surface (solid lines) and the Fermi surface shifted by  $-q$  (dashed lines). Nesting parts of the Fermi surface can only have a strong effect on the phonons if they occur in  $k$ -space regions with significant electron–phonon coupling (dark/brown spots). While the  $\tilde{g}$  from DFPT is fully screened, the partially screened  $g$  from constrained DFPT (cDFPT)<sup>8</sup> excludes low-energy electronic screening (precisely, from within the isolated band at the Fermi level). Together with the bare electronic susceptibility  $\chi_0$ , they determine the phonon self-energy  $\Pi = g^* \chi_0 \tilde{g}$  responsible for the instabilities in the phonon dispersion. This analysis is equivalent to the fluctuation diagnostics in Ref. 9. The electron–phonon coupling has been obtained via the EPW code<sup>10,11</sup>.

In Fig. 2a of the manuscript, we can observe two main instabilities in the acoustic phonon dispersion of monolayer 1T-VS<sub>2</sub> from density functional perturbation theory (DFPT): one in the longitudinal branch at  $q \approx 1/2 \overline{\Gamma M}$  and one in the transverse branch at  $q \approx 2/3 \overline{\Gamma K}$ . A mode with momentum  $q$  will be favoured if there is a large electron–phonon coupling matrix element connecting momenta  $k$  and  $k + q$  close to the Fermi surface. These nesting conditions are investigated in Fig. S4. In the longitudinal case, shown in Fig. S4a, we have almost perfect Fermi-surface nesting together with a strong electron–phonon coupling (cf. Fig. 5c, d of Ref. 12 for the case of 1T-VSe<sub>2</sub>). This  $q$  point is compatible with the formation of a  $4 \times 4$  CDW, as found, e.g., in bulk VSe<sub>2</sub><sup>13</sup>. Interestingly, despite these favorable conditions, this is not the preferred ground state of monolayer VS<sub>2</sub>. Instead, a CDW



with a wavevector near  $\mathbf{q} = 2/3 \overline{\Gamma\text{K}}$  and  $\mathbf{q} = 9/14 \overline{\Gamma\text{K}}$  develops, which features only approximate nesting and a slightly reduced coupling strength, as seen in Fig. S4b, c. As discussed in the main text, the formation of the CDW can only be understood considering non-linear mode–mode coupling. Phonon modes that appear stable in the harmonic approximation contribute significantly to the final atomic displacements, especially the longitudinal–acoustic modes for twice the momenta of the unstable modes, i.e.,  $\mathbf{q} = \text{M}$ ,  $\mathbf{q} = 9/7 \overline{\Gamma\text{K}}$ , and  $\mathbf{q} = 4/3 \overline{\Gamma\text{K}}$ , see Fig. S4d–f. For both the harmonic (Fig. S4b, c) and the higher-order contributions (Fig. S4e, f) to the experimentally observed CDW, we find a similar situation of partially overlapping Fermi pockets in  $\mathbf{k}$ -space regions of considerable coupling, except that different pairs of pockets are involved.

**Figure S5: Born–Oppenheimer energy surface in TaS<sub>2</sub>**

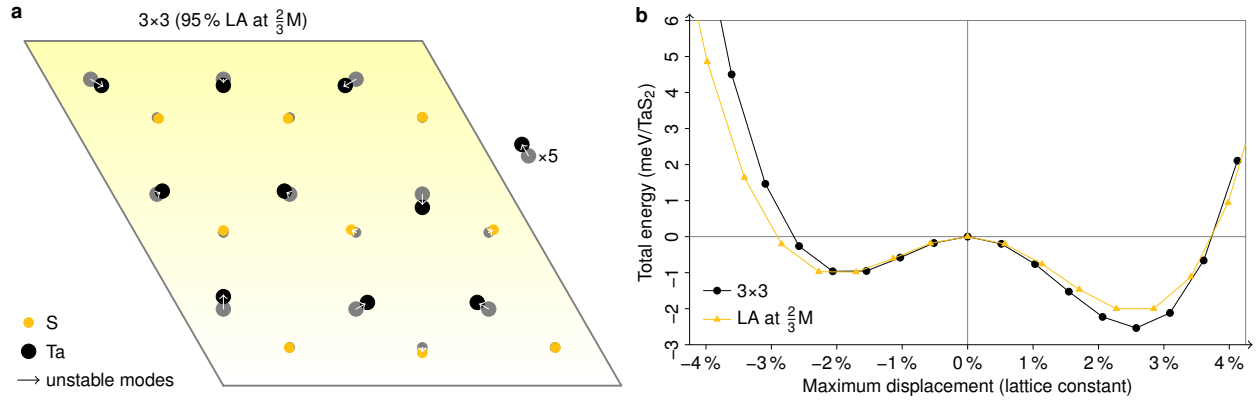


**Figure S5: a** CDW distortion in monolayer 2H-TaS<sub>2</sub> and **b** corresponding Born–Oppenheimer energy surface. Full circles indicate atomic positions and energies for displacements in the direction of the relaxed structure, arrows and triangle marks those for the projection onto the unstable longitudinal–acoustic phonon modes at the six wavevectors  $\mathbf{q} = 2/3 \bar{\Gamma}M$ . The relaxed atomic displacements have been amplified by a factor of five for better visibility.

While the experimentally observed CDW in VS<sub>2</sub> can only be explained by the nonlinear coupling between soft and stable phonon modes, the  $3 \times 3$  CDW in the trigonal–prismatic TMDCs is an example of a lattice instability that is determined essentially by a single unstable phonon mode. Analogous to Fig. 2b–e, Fig. S5 shows the  $3 \times 3$  CDW structure and the corresponding Born–Oppenheimer energy surface of monolayer 2H-TaS<sub>2</sub> from DFT: Here, the distortion along the leading unstable phonon normal-mode coordinate largely captures the energy gain associated with the full CDW relaxation. We used the same computational parameters as in Ref. 9.

**Figure S6: Phonon dispersion, nesting conditions, and electron–phonon coupling in 1T-VTe<sub>2</sub>**

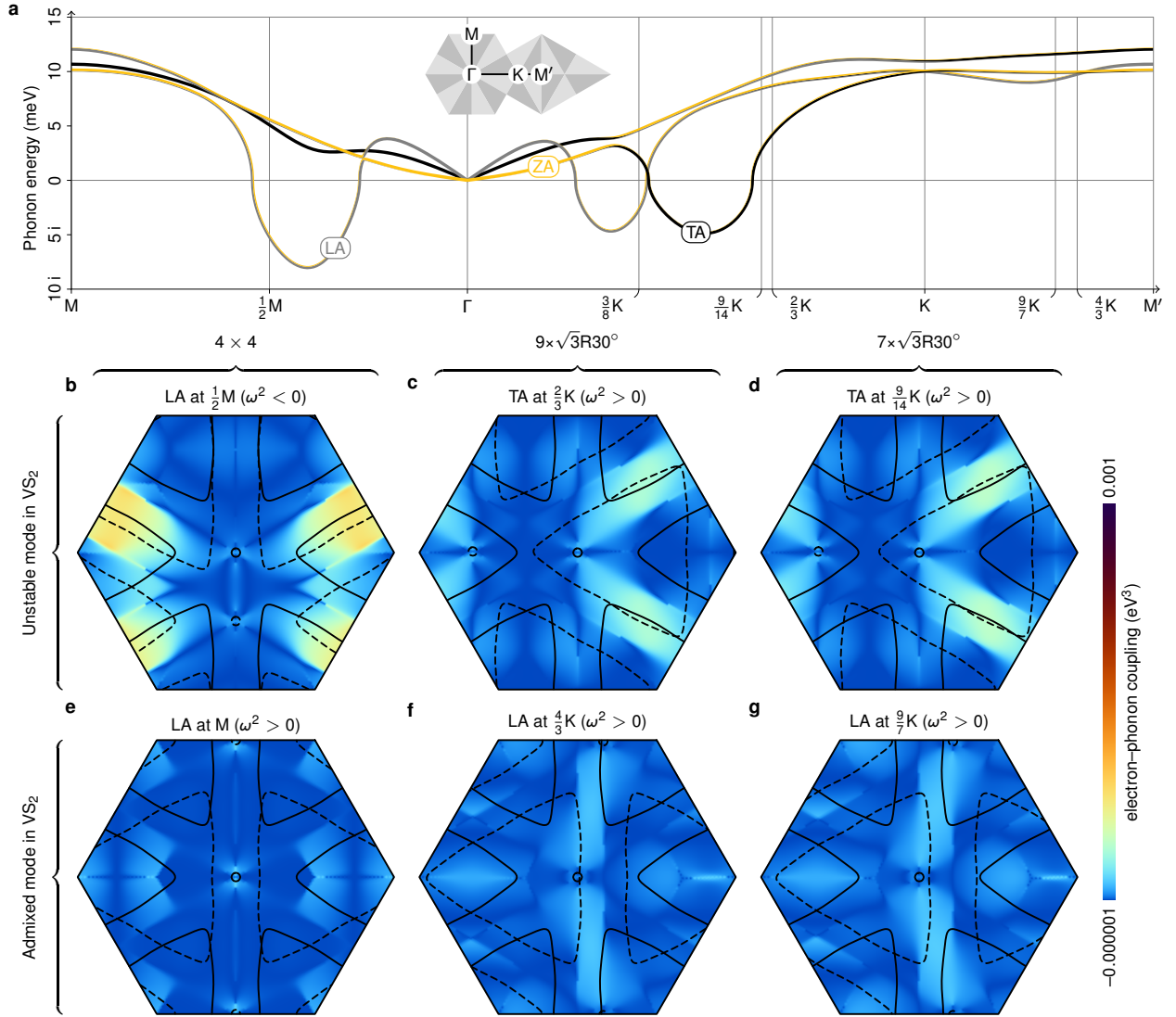


**Figure S6: a** Phonon dispersion of monolayer 1T-VTe<sub>2</sub>. **b–g** Corresponding electron–phonon coupling  $2\omega_{\mathbf{q}}g_{\mathbf{k}+\mathbf{q},\mathbf{k}}\tilde{g}_{\mathbf{k},\mathbf{k}+\mathbf{q}}$  together with the  $\mathbf{k}$  and  $\mathbf{k} + \mathbf{q}$  Fermi surfaces (cf. Fig. S4).

The phonon dispersion of monolayer 1T-VTe<sub>2</sub> obtained from DFPT is shown in Fig. S6a. We find similar lattice instabilities as in the case of 1T-VS<sub>2</sub> (cf. Fig. 2a of the main text), albeit shifted to smaller  $|\mathbf{q}|$ . This shift, which is more pronounced for the transverse–acoustic instability in the  $\overline{\Gamma\text{K}}$  direction than for the longitudinal–acoustic instability in the  $\overline{\Gamma\text{M}}$  direction, can be traced back to differences in the Fermi surface (topology) rather than in the electron–phonon coupling, see Fig. S6b–g: Instead of the cigar-shaped electron pockets around the M points in 1T-VS<sub>2</sub> (cf. Fig. S4), we find triangular hole pockets around the K points (as well as a small hole pocket at  $\Gamma$ ) in 1T-VTe<sub>2</sub>. In the latter case, the approximately parallel segments of the Fermi surface are closer together.

**Table S1: CDW energy gains in VS<sub>2</sub> vs VTe<sub>2</sub>**

**Table S1:** Comparison of maximum atomic displacements and energy gains upon CDW formation for different materials and periodicities from DFT (PBE). All energies refer to a single VX<sub>2</sub> unit; the reference for the displacements is the lattice constant.

|                              | 1T-VS <sub>2</sub> |          | 1T-VTe <sub>2</sub> |          |
|------------------------------|--------------------|----------|---------------------|----------|
| $4 \times 4$                 | 4 %                | 3.4 meV  | 13 %                | 34.2 meV |
| $7 \times \sqrt{3}R30^\circ$ | 8 %                | 22.7 meV | 6 %                 | 2.5 meV  |

To compare the energy gains associated with CDW formation in 1T-VS<sub>2</sub> and in 1T-VTe<sub>2</sub> for the different periodicities, we performed structural relaxations on corresponding supercells in the framework of DFT (PBE). The energy gains reported in Table S1 show that in 1T-VS<sub>2</sub> the  $7 \times \sqrt{3}R30^\circ$  CDW is favored over the  $4 \times 4$  CDW; in 1T-VTe<sub>2</sub> vice versa. The DFT prediction is thus in line with experimental observation for both materials.

**Figure S7: Compression of electronic spectrum**

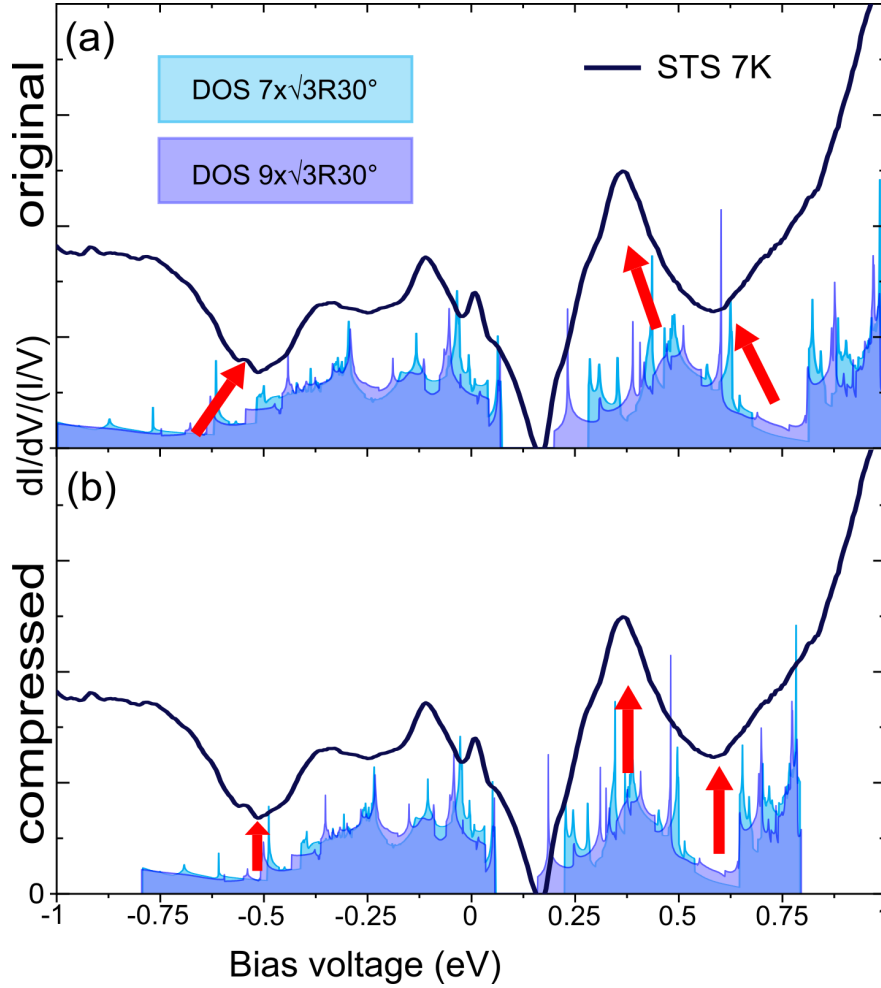


**Figure S7:** Compression of experimental spectrum relative to DFT-calculated DOS. In **a**, the 7 K spectrum from the main manuscript is compared to the calculated DOS for the  $7 \times \sqrt{3}R30^\circ$  and  $9 \times \sqrt{3}R30^\circ$  unit cells. In **b**, the calculated DOS is compressed to about 80 % of its original width. The red arrows in **a**, **b** indicate three major features in the spectrum and DOS that can be harmonized between them when the DOS is compressed.

In Fig. 4a of the main text, the DOS from DFT appears to be wider than the experimental spectrum. Dynamic electronic correlation effects beyond DFT are a possible source of this discrepancy, since they can lead to band renormalization<sup>14</sup>. More precisely, they effect a mass enhancement of the electrons, i.e., the quasi-particle dispersions become flatter than what is expected from theories like DFT. In the case of purely local correlations<sup>15</sup>, this effect is described by a single renormalization factor  $Z$  or the corresponding mass enhancement factor  $1/Z$ . Figure S7 shows that we obtain a good match between experimental and theoretical spectra by setting  $Z = 0.8$ . This is indicative of moderate electronic correlations. For comparison, examples range from diverging mass enhancement at Mott–Hubbard transitions, via mass enhancement factors of about 10 to 1000

in Kondo or heavy fermion systems, to enhancement factors between 1 and 10 in transition-metal compounds like metallic chromium or iron-based superconductors. The mass enhancement factor of  $1/Z \approx 1.25$  puts  $\text{VS}_2$  at similar electronic correlation strengths as, e.g., metallic chromium<sup>16</sup>.

The rise in the normalized  $dI/dV$  beyond  $-0.5$  eV can be attributed to contributions from the graphene/Ir(111) substrate, which can come to dominate the signal for large  $V$  when the  $\text{VS}_2$  has a small DOS. In this case, the graphene spectrum (not shown) diverges beyond the Ir(111) surface state at  $-190$  meV.

**Figure S8: Suppression of CDW Fourier intensity within the gap**

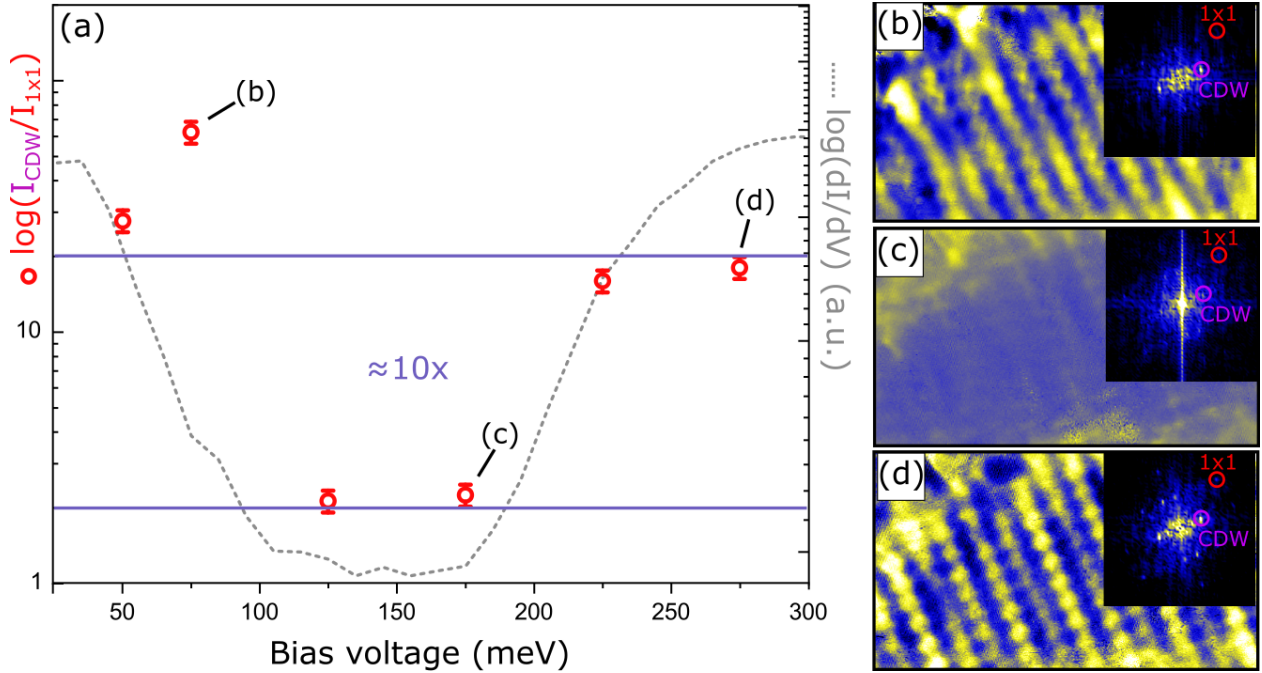


**Figure S8: Suppression of CDW within the gap.** **a** Logarithmic plot of the CDW intensity in the Fourier transform of  $dI/dV$  conductance maps, normalized to the  $1 \times 1$  lattice intensity. Additionally, a  $dI/dV$  spectrum is plotted in order to indicate the location and width of the gap. **b–d**  $dI/dV$  conductance maps taken at the voltages indicated in **a**. Measurement settings: (maps)  $9.5 \times 5.5 \text{ nm}^2$ ,  $I_t = 0.3 \text{ nA}$ , except for the map at 50 meV, which is taken at  $I_t = 0.6 \text{ nA}$ ; ( $dI/dV$  spectrum)  $f = 777.7 \text{ Hz}$ ,  $I_t = 0.4 \text{ nA}$ ,  $V_{\text{r.m.s.}} = 6 \text{ meV}$ . All data taken at  $T = 7 \text{ K}$ .

Apart from the different charge distributions on either side of the gap discussed in the main manuscript,  $dI/dV$  maps taken within the gap show a clear suppression of the CDW. For a quantitative analysis, we have Fourier analyzed the  $dI/dV$  maps and normalized the CDW peak in the Fourier spectrum with respect to the  $1 \times 1$  lattice peak intensity. The resulting value  $R = I_{\text{CDW}}/I_{1 \times 1}$  is observed to fall by an order of magnitude within the gap. Since a gap of other than CDW origin would have the same value of  $R$  in- and outside of the gap region<sup>17</sup>, this is another clear indication of the relation between gap and CDW.

**Figure S9: Bands along extended Brillouin-zone path**

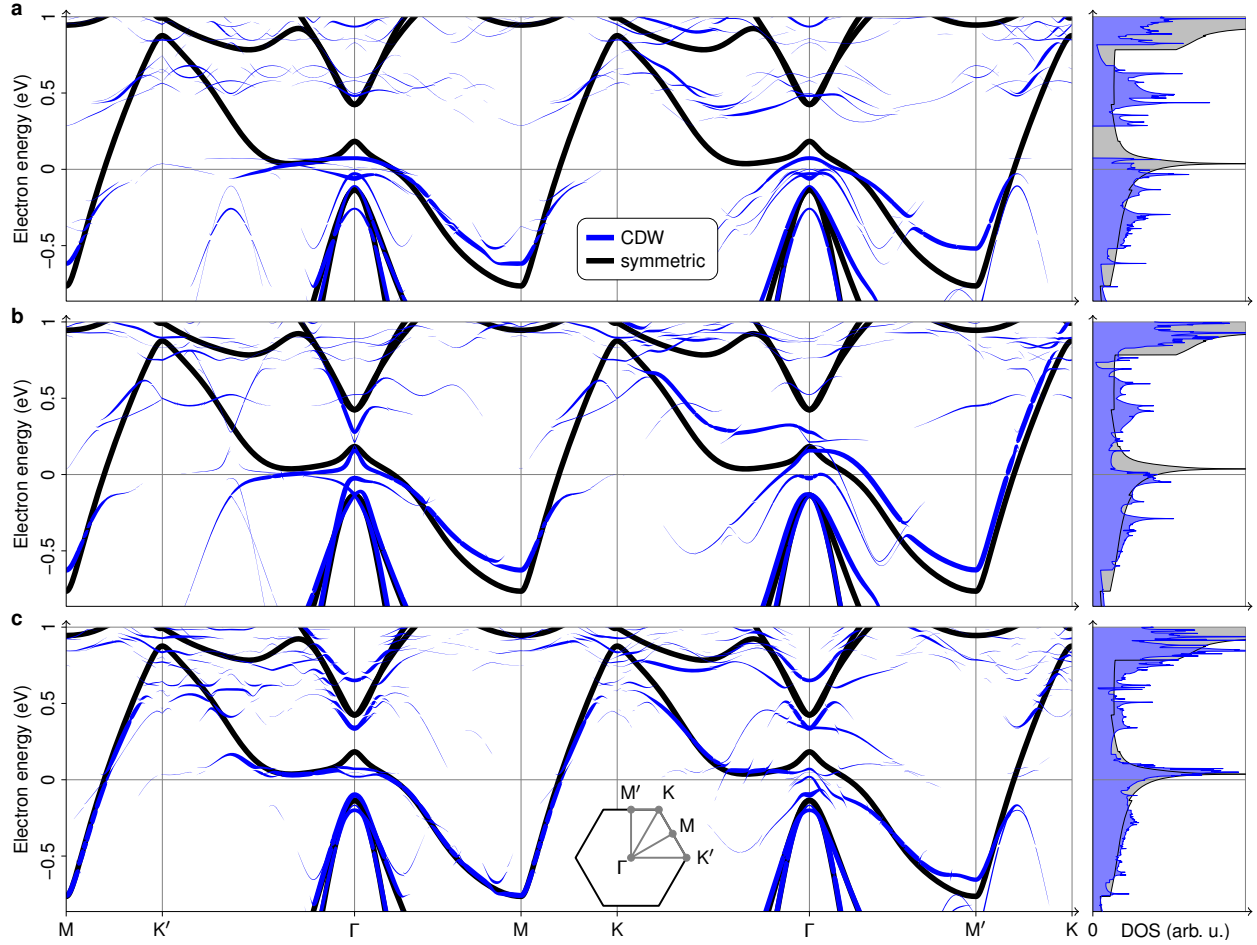


**Figure S9:** Electronic band structure along an extended Brillouin-zone path and DOS of monolayer 1T-VS<sub>2</sub> for **a** the full  $7 \times \sqrt{3}R30^\circ$  CDW displacements, **b** their projection onto unstable phonon modes, and **c** the orthogonal complement.

In Fig. 5a of the manuscript, we show the electronic band structure of monolayer 1T-VS<sub>2</sub> in the  $7 \times \sqrt{3}R30^\circ$  phase along a selected high-symmetry path  $\Gamma$ -M-K- $\Gamma$  of the undistorted phase only. Once the distortion breaks the  $C_3$  symmetry, this path is not representative of the full Brillouin zone anymore. For completeness, in Fig. S9a, we thus reproduce the respective data along an extended path, again supplemented with the DOS. In Fig. S9b,c, we show the analogous results for the projection of the displacement onto the soft transverse-acoustic phonon modes at  $\mathbf{q} = \pm 9/14 \bar{\Gamma}\bar{K}$  and the orthogonal complement. There are some salient differences between the electrons for the full and partial CDW displacement. In Fig. S9b, the gap between M' and K is missing; in turn, in Fig. S9c, there is no gap between M and K' as well as M and K. The combination of both displacement components is needed to open a full gap.



**Figure S10: Preservation of states at the Fermi level**

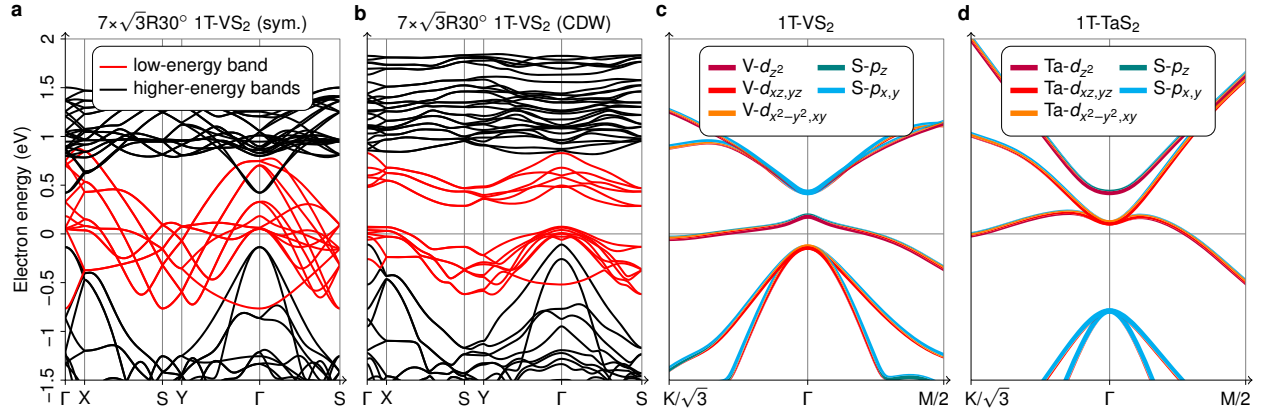


**Figure S10: a, b** Band structure of symmetric and distorted 1T-VS<sub>2</sub> along path through Brillouin zone corresponding to  $7 \times \sqrt{3}R30^\circ$  cell. The low-energy band is half-filled and splits into seven four-fold (including spin) bands between X and S. Thus, there must be  $1/7$  unoccupied states per V atom below the gap. **c, d** Orbital-resolved low-energy electron dispersion of 1T-TaS<sub>2</sub> and 1T-VS<sub>2</sub> near  $\Gamma$ . In the case of 1T-VS<sub>2</sub> there is an avoided crossing between V-*d* and S-*p<sub>x,y</sub>* bands.

The CDW does not create a complete gap at the Fermi level. For the commensurate structures used to approximate the incommensurate CDW, it is the combination of the electron count and the symmetry of the unit cell that guarantees a partially filled band, i.e., a metallic DOS. A complete gap at the Fermi level in the CDW would require the splitting of bands that must be degenerate by symmetry of the CDW structures (Fig. S10a, b), i.e., further symmetry breaking.

The particular form of the remaining spectral weight at the Fermi level resembling a downwards dispersing parabola around  $\Gamma$  in the CDW state (cf. Fig. 5) can be understood in terms of orbital band characters: In 1T-VS<sub>2</sub>, we find an avoided crossing of V-*d* and S-*p<sub>x,y</sub>* bands in the relevant region and thus a significant hybridization between these states (Fig. S10c). This is opposed to, e.g., the case of 1T-TaS<sub>2</sub>, where the S-*p<sub>x,y</sub>* states are much lower in energy (Fig. S10d). Now, while the *d*-type bands are heavily reconstructed due to the CDW, the *p* orbitals are less affected and can contribute to a new Fermi surface in the case of 1T-VS<sub>2</sub> in contrast to 1T-TaS<sub>2</sub>.

**Figure S11: XMCD sample morphology**

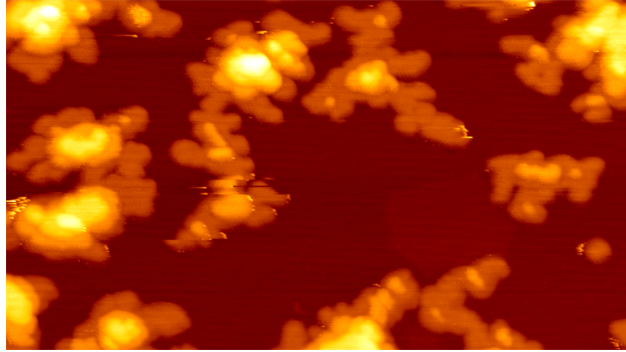


**Figure S11:** Magnetic properties of VS<sub>2</sub>: STM topograph illustrating the sample morphology of the XMCD measured sample. Image size:  $100 \times 50 \text{ nm}^2$ .

In the main manuscript, we describe the magnetic properties of VS<sub>2</sub> as measured by x-ray absorption spectroscopy (XAS) and x-ray magnetic circular dichroism (XMCD). Figure S11 displays the sample morphology of the investigated sample. Like the samples shown in the main text, the island shape is dendritic. By comparison to substrate step edges, the monolayer height is measured to be  $7 \text{ \AA}$ . The sample has a monolayer coverage of about 40 %. Distinct height levels indicate three layers.

**Figure S12: DOS for SDW**

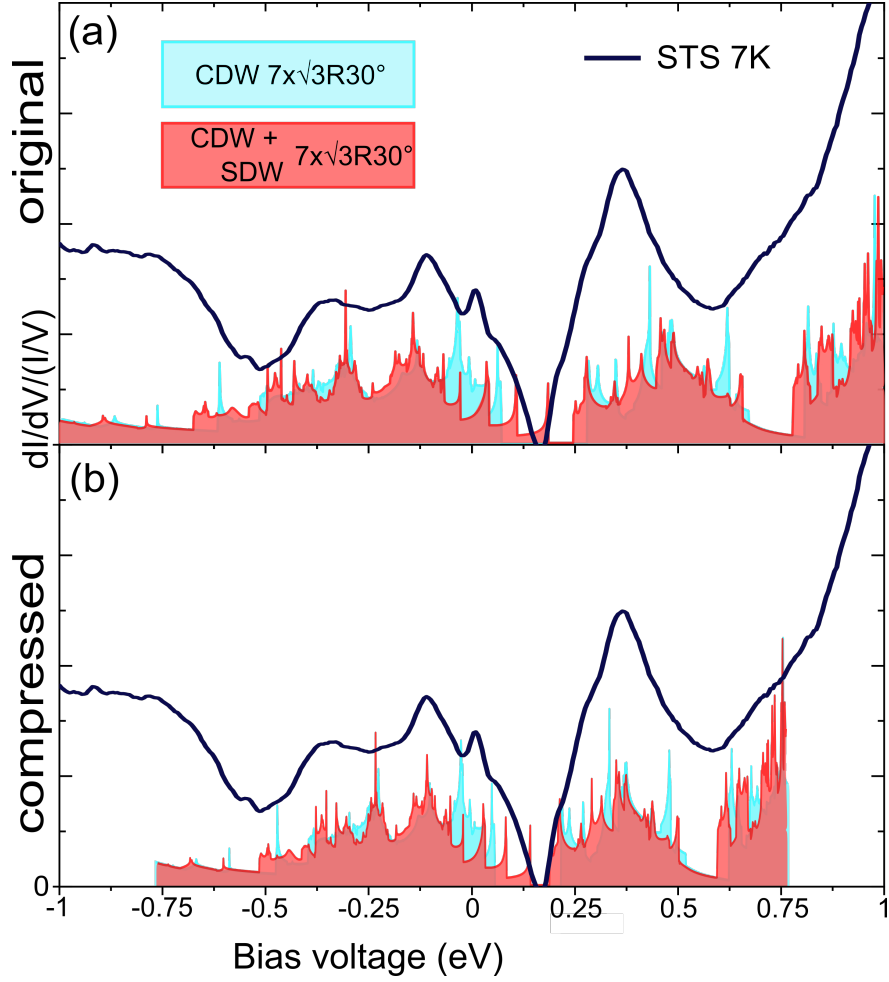


**Figure S12: a**  $dI/dV$  spectra taken with a Au tip on monolayer  $VS_2$  at 7 K along with DFT calculated CDW DOS with (red) and without (cyan) SDW. **b** The same data after compressing calculated DOS to 80% of original size.

In Fig. S12a, we show the DOS of the CDW structure with and without spin density wave (SDW), along with the experimental  $dI/dV$  spectra. The most prominent difference in the DOS is the reduction of the gap size. For the  $7 \times \sqrt{3}R30^\circ$  structure, the gap shrinks from 0.21 eV to 0.06 eV when the CDW is coupled to a SDW. Since the CDW gap is indeed much larger in DFT than the experimental gap, this can be considered as an additional argument for the simultaneous presence of a SDW. Taking into account the compression of the experimental data, discussed under Fig. S7, the DOS of the coupled CDW–SDW is in even better agreement with the experimental spectra, as seen in Fig. S12b.

**Figure S13: Comparison of DFT results with literature data for VSe<sub>2</sub>**

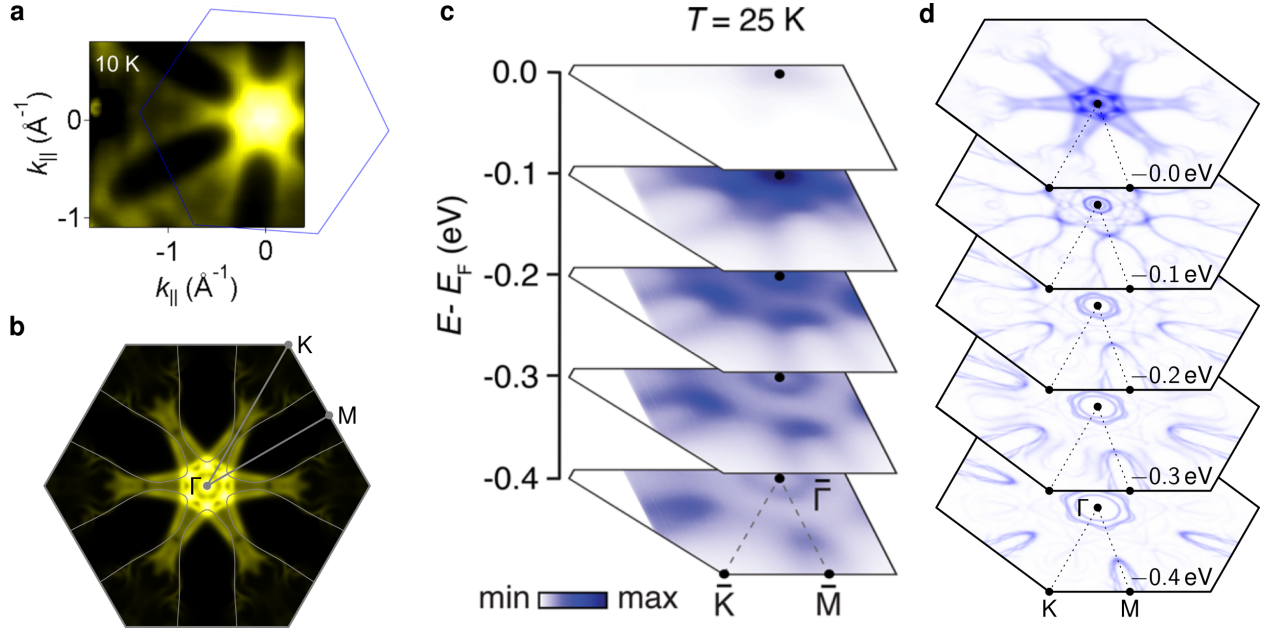


**Figure S13:** Fermi surface of  $7 \times \sqrt{3}R30^\circ$  CDW of monolayer 1T-VSe<sub>2</sub> averaged over regions of different CDW orientations and comparison to experiment. **a** Fermi surface reprinted with permission from Ref. 2 © 2018 American Physical Society. **b** Symmetrized Fermi surface calculated in this work. **c** Energy isolines reprinted with permission from Ref. 7 © 2018 American Chemical Society. **d** Symmetrized energy isolines calculated in this work.

In order to compare our DFT results for monolayer VSe<sub>2</sub> to existing ARPES studies, we have averaged our calculated Fermi surface of VSe<sub>2</sub> in the  $7 \times \sqrt{3}R30^\circ$  CDW phase over all domains of the CDW with respect to the lattice. In this way, many of the familiar ARPES characteristics of VSe<sub>2</sub> are uncovered. If we compare to VSe<sub>2</sub> systems where only the  $7 \times \sqrt{3}R30^\circ$  CDW was observed<sup>2,3</sup>, we see that the experimental data in Fig. S13a, taken from Ref. 2, shows excellent agreement with our calculated Fermi surface in Fig. S13b. In particular, we observe the formation of gaps between M and K, while the rest of the Fermi surface remains intact. The apparent persistence of the six cigar-shaped electron pockets and the appearance of the hole pocket around  $\Gamma$  are visible in both theory and experiment. That the ARPES measurements show such small changes during the transition to the CDW phase can therefore be understood as stemming mostly from the fact that it is an averaging technique. More subtle changes to the band structure around  $\Gamma$  and the elliptic electron pockets cannot easily be compared by eye. All in all, our theoretical studies match very well to experimental ARPES reports of VSe<sub>2</sub> in the  $7 \times \sqrt{3}R30^\circ$  phase<sup>2,3</sup>.

It must however be noted that most publications on VSe<sub>2</sub> find, in contrast to our prediction, a full gap at the Fermi level<sup>1,4,6,7</sup>. Monolayer VSe<sub>2</sub>, especially in the light of recent works<sup>12,18,19</sup>, seems to have a strong substrate-dependence. It is therefore likely that our calculation, which is based on freestanding VSe<sub>2</sub>, does not capture the intricacies of all experimental systems. At the Fermi surface, an (additional)  $4 \times 1$  CDW found on some substrates<sup>1,6,12,19</sup>, might induce an

insulating state. A possible cause for the presence of different and competing CDW orders might be substrate-induced strain<sup>20</sup>, which is not included in our DFT calculations. Fig. S13c shows the Fermi surface and constant-energy contours at higher binding energies of a VSe<sub>2</sub> system where the Fermi surface is fully gapped at 25 K, taken from Ref. 7. In this case, though our calculation in Fig. S13d does not predict the fully gapped surface, we see that it captures the features of the band structure away from the Fermi level quite well. The dissimilarities between VSe<sub>2</sub> systems with different CDW orders might therefore pertain mostly to the Fermi surface and the unoccupied states.

## References

1. Duvjir, G. *et al.* Emergence of a metal–insulator transition and high-temperature charge-density waves in VSe<sub>2</sub> at the monolayer limit. *Nano Lett.* **18**, 5432 (2018). URL <https://doi.org/10.1021/acs.nanolett.8b01764>.
2. Chen, P. *et al.* Unique gap structure and symmetry of the charge density wave in single-layer VSe<sub>2</sub>. *Phys. Rev. Lett.* **121**, 196402 (2018). URL <https://doi.org/10.1103/PhysRevLett.121.196402>.
3. Coelho, P. M. *et al.* Charge density wave state suppresses ferromagnetic ordering in VSe<sub>2</sub> monolayers. *J. Phys. Chem. C* **123**, 14089 (2019). URL <https://doi.org/10.1021/acs.jpcc.9b04281>.
4. Wong, P. K. J. *et al.* Evidence of spin frustration in a vanadium diselenide monolayer magnet. *Adv. Mater.* **31**, 1901185 (2019). URL <https://doi.org/10.1002/adma.201901185>.
5. Bonilla, M. *et al.* Strong room-temperature ferromagnetism in VSe<sub>2</sub> monolayers on van der Waals substrates. *Nat. Nanotechnol.* **13**, 289 (2018). URL <https://doi.org/10.1038/s41565-018-0063-9>.
6. Chua, R. *et al.* Can reconstructed Se-deficient line defects in monolayer VSe<sub>2</sub> induce magnetism? *Adv. Mater.* **32**, 2000693 (2020). URL <https://doi.org/10.1002/adma.202000693>.
7. Feng, J. *et al.* Electronic structure and enhanced charge-density wave order of monolayer VSe<sub>2</sub>. *Nano Lett.* **18**, 4493 (2018). URL <https://doi.org/10.1021/acs.nanolett.8b01649>.
8. Nomura, Y. & Arita, R. Ab initio downfolding for electron-phonon-coupled systems: Constrained density-functional perturbation theory. *Phys. Rev. B* **92**, 245108 (2015). URL <https://doi.org/10.1103/PhysRevB.92.245108>.
9. Berges, J., van Loon, E. G. C. P., Schobert, A., Rösner, M. & Wehling, T. O. Ab initio phonon self-energies and fluctuation diagnostics of phonon anomalies: Lattice instabilities from Dirac pseudospin physics in transition metal dichalcogenides. *Phys. Rev. B* **101**, 155107 (2020). URL <https://doi.org/10.1103/PhysRevB.101.155107>.
10. Giustino, F., Cohen, M. L. & Louie, S. G. Electron-phonon interaction using Wannier functions. *Phys. Rev. B* **76**, 165108 (2007). URL <https://doi.org/10.1103/PhysRevB.76.165108>.
11. Poncé, S., Margine, E., Verdi, C. & Giustino, F. EPW: Electron–phonon coupling, transport and superconducting properties using maximally localized Wannier functions. *Comput. Phys. Commun.* **209**, 116 (2016). URL <https://doi.org/10.1016/j.cpc.2016.07.028>.

12. Chua, R. *et al.* Coexisting charge-ordered states with distinct driving mechanisms in monolayer VSe<sub>2</sub> (2021). URL <https://arxiv.org/abs/2104.12420>.
13. Williams, P. M. Phase transitions and charge density waves in the layered transition metal dichalcogenides. In Lévy, F. (ed.) *Crystallography and Crystal Chemistry of Materials with Layered Structures* (Reidel, Dordrecht, 1976). URL [https://doi.org/10.1007/978-94-010-1433-5\\_2](https://doi.org/10.1007/978-94-010-1433-5_2).
14. Giuliani, G. & Vignale, G. *Quantum Theory of the Electron Liquid* (Cambridge University Press, Cambridge, 2005). URL <https://doi.org/10.1017/CBO9780511619915>.
15. Georges, A., Kotliar, G., Krauth, W. & Rozenberg, M. J. Dynamical mean-field theory of strongly correlated fermion systems and the limit of infinite dimensions. *Rev. Mod. Phys.* **68**, 13 (1996). URL <https://doi.org/10.1103/RevModPhys.68.13>.
16. Qazilbash, M. M. *et al.* Electronic correlations in the iron pnictides. *Nat. Phys.* **5**, 647 (2009). URL <https://doi.org/10.1038/nphys1343>.
17. Ugeda, M. M. *et al.* Characterization of collective ground states in single-layer NbSe<sub>2</sub>. *Nat. Phys.* **12**, 92 (2016). URL <https://doi.org/10.1038/nphys3527>.
18. Zong, J. *et al.* Observation of multiple charge density wave phases in epitaxial monolayer 1T-VSe<sub>2</sub> film. *Research Square* (2021). URL <https://doi.org/10.21203/rs.3.rs-498840/v1>.
19. Duvjir, G. *et al.* Multiple charge density wave phases of monolayer VSe<sub>2</sub> manifested by graphene substrates. *Nanotechnology* **32**, 364002 (2021). URL <https://doi.org/10.1088/1361-6528/ac06f3>.
20. Si, J. G. *et al.* Origin of the multiple charge density wave order in 1T-VSe<sub>2</sub>. *Phys. Rev. B* **101**, 235405 (2020). URL <https://doi.org/10.1103/PhysRevB.101.235405>.